POLITECNICO DI TORINO
Repository ISTITUZIONALE

A Chemical Reactor Network methodology for estimating NOx emissions under non-premixed lean hydrogen combustion with water injection

Original
A Chemical Reactor Network methodology for estimating NOx emissions under non-premixed lean hydrogen combustion with water injection / Folcarelli, L., Concetti, R., Cozzi, F., Ferrero, A., Masseni, F., Pastrone, D., Hasslberger, J., Klein, M.. - In: INTERNATIONAL JOURNAL OF HYDROGEN ENERGY. - ISSN 0360-3199. - ELETTRONICO. - 168:(2025), pp. 1-15. [10.1016/j.ijhydene.2025.150561]

Availability:
This version is available at: 11583/3006486 since: 2026-01-12T23:15:47Z

Publisher:
Elsevier

Published
DOI:10.1016/j.ijhydene.2025.150561

Terms of use:

This article is made available under terms and conditions as specified in the corresponding bibliographic description in the repository

Publisher copyright

(Article begins on next page)

16 October 2026

International Journal of Hydrogen Energy 168 (2025) 150561

Contents lists available at ScienceDirect

International Journal of Hydrogen Energy

journal homepage: www.elsevier.com/locate/he

A Chemical Reactor Network methodology for estimating NO_x emissions under non-premixed lean hydrogen combustion with water injection

Lorenzo Folcarelli [a,*], Riccardo Concetti [b], Fabio Cozzi [c], Andrea Ferrero [a], Filippo Masseni [a], Dario Pastrone [a], Josef Hasslberger [b], Markus Klein [b]

[a] Department of Mechanical and Aerospace Engineering, Politecnico di Torino, Corso Duca degli Abruzzi, 24, Torino, 10129, Italy
[b] Department of Aerospace Engineering, University of the Bundeswehr Munich, Werner-Heisenberg-Weg, 39, Neubiberg, 85577, Germany
[c] Department of Energy, Politecnico di Milano, Via Lambruschini, 4, Milano, 20156, Italy

ARTICLE INFO

Keywords:
Computational Fluid Dynamics CFD
Chemical Reactor Network CRN
NO_x emission
Non-premixed lean combustion
Water injection
Hydrogen

ABSTRACT

This study investigates the ability of Chemical Reactor Network (CRN) methodologies in predicting NO_x reduction through water injection in a lean non-premixed hydrogen combustor for a given outlet flame temperature. A new methodology for creating a chemical reactor network to analyze emissions is proposed and validated. The novelty lies in the definition of the connections between the different reactors composing the network using an optimization algorithm. This approach allows the prediction of emissions without the need for complete knowledge of the flow field of the combustor through PIV or high-fidelity CFD simulations. The proposed method proves to be a reliable and computationally efficient framework for predicting hydrogen combustion emissions, achieving thousand-fold computational savings over CFD while maintaining prediction accuracy on the NO_x emissions within experimental uncertainty. The results are validated through comparisons with CFD simulations, which are first assessed against experimental data without water injection, demonstrating CFD's effectiveness in this scenario. The CRN, trained without water injection, successfully applies to the water injection cases, demonstrating its predictive capability beyond the training conditions.

1. Introduction

In recent years, hydrogen has garnered significant attention as a potential energy carrier in the transition to a net-zero carbon society. Particularly, with the advent of green hydrogen production, this fuel could play a role in a fully circular economy [1, 2]. Although carbon dioxide (CO_2) emissions can ideally be avoided, nitrogen oxides (NO_x, here comprising NO and NO_2) emissions still persist and may even increase compared to kerosene due to higher flame temperatures at a given equivalence ratio. Lean combustion and the use of water injection are proposed as means to reduce these emissions.

The potential for employing liquid water and steam injection in combustion systems has historically been considered due to its capacity to enhance overall power output and fuel efficiency [3]. In recent years, this technique has gained attention as a strategy for reducing harmful emissions, particularly within frameworks such as MILD combustion [4] and Exhaust Gas Recirculation (EGR), which aim to lower the maximum system temperature. This approach is viewed as promising for reducing NO_x emissions and other harmful by-products, as documented in the literature [5–8]. There are examples of its potential application, such as the WET engine configuration proposed by MTU in the aerospace sector [9] or the Hydrogen Steam and Inter-Cooled Turbine Engine (HySITE) proposed by Pratt & Whitney [10].

The above mentioned reduction of NO_x stems from various mechanisms. Various studies [11–15] have investigated the three primary effects of water interaction with flames:

1. *Cooling effect*: Heat is extracted during the phase change of liquid water, reducing the heat released from combustion. Furthermore, cooling is due to high c_p of steam compared to other gases, particularly air.
2. *Dilution effect*: Steam, directly injected or produced from evaporation reduces the mass fraction of reactants, lowering the system's heat release per unit mass.
3. *Chemical effect*: Water exhibits high collision efficiency in third-body reactions. Moreover, as thermodynamic effect, shifts the equilibrium conditions as it is also one of the major combustion products.

* Corresponding author.
E-mail address: lorenzo.folcarelli@polito.it (L. Folcarelli).

https://doi.org/10.1016/j.ijhydene.2025.150561
Received 9 April 2025; Received in revised form 11 June 2025; Accepted 17 July 2025
Available online 21 August 2025
0360-3199/© 2025 The Authors. Published by Elsevier Ltd on behalf of Hydrogen Energy Publications LLC. This is an open access article under the CC BY license (http://creativecommons.org/licenses/by/4.0/).

In liquid water injection, the cooling effect is dominant, while the chemical effect can be considered secondary. At the same time, in steam injection, the cooling effect is generally less significant compared to the dilution and chemical effects. Even if NO_x reduction can be achieved through the decrease of temperature caused by the steam, the chemical effect of water is capable of decreasing NO_x concentration even at constant temperatures, as demonstrated by Concetti et al. [16]. This phenomenon arises from the impact on flame structure and the redistribution of radicals, particularly atomic oxygen (O), which influences the N_2O mechanism, as highlighted in Göke and Paschereit [5], Göke et al. [6]. Early research by Koroll and Mulpuru [17] on the high collision efficiency of water in flame structures showed that when hydrogen/oxygen premixed flames are diluted with steam, the reduction in flame speed is less than the value predicted if water was assumed to be inert. This effect is primarily due to a specific third-body reaction:

$$H + O_2 + M \leftrightarrow HO_2 + M \quad (1)$$

The importance of this reaction has also been recognized in studies by Lamioni et al. [18] and Attili et al. [19], where it has been associated with a chain-breaking reaction competing with a non-third-body chain-branching reaction. The balance between these reactions is temperature-dependent and influenced by the presence of species like water that affect third-body reaction dynamics. The relevance of the third-body reactions efficiency of water on the flame speed has also been stressed in the study of Lyu et al. [20], where it has been considered in combination with pressure effects.

Beyond being carbon-free, hydrogen offers several advantages, including high specific energy, with a lower heating value of 120 MJ/kg [21], broad availability, and applicability across a wide range of conditions. However, there are also substantial safety concerns related to hydrogen's volatility, difficulty in maintaining liquid form, low volumetric density (requiring larger storage volumes), and high reactivity, which necessitate stringent precautions throughout its use. Given these challenges, it is crucial to develop a deep understanding of hydrogen combustion, especially for practical applications. Numerical simulations at various levels of fidelity can be instrumental in achieving this. This study aims to propose a reliable yet computationally efficient numerical framework for predicting harmful emissions, specifically NO_x, which are the primary pollutants in hydrogen combustion with air due to the high temperatures reached. Although accounting for pollutant species such as NO_x during numerical simulations is now feasible, it remains computationally expensive and impractical for extensive parametric studies during the design process. The conventional approach in Reynolds-averaged numerical simulations (RANS) involves estimating these chemical species in post-processing, a technique justified by the long timescales of nitrogen chemistry and the minimal impact of NO_x formation on temperature and other chemical fields [22]. However, this approach requires new RANS simulations for every parametric variation, even minor ones, leading to higher computational costs during the design process.

Recent research has focused on developing techniques that represent combustion devices using ensembles of 0D ideal gas reactors [5, 23–27]. The general approach involves performing a CFD calculation with a simplified chemical kinetic mechanism, then dividing the computational domain into subdomains with similar thermochemical characteristics. Each subdomain is modeled as a 0D reactor, and fluxes between subdomains are derived from CFD results. This reactor network can then be used with a more comprehensive chemical mechanism to capture nitrogen chemistry and other pollutants [23, 24].

Recently, the development of new machine learning and optimization techniques improved the design methodology of the Chemical Reactor Network (CRN) [28, 29]. The present study aims to further develop the CRN design methodology, proposing an approach that does not rely on new CFD simulations for every design modification and does not rely on a large amount of data from high-fidelity simulations or experimental measurements. Instead, it leverages the general flow behavior of the system, dividing the combustion chamber based on recirculation zones. The fluxes in this methodology are optimized using a mono-objective Particle Swarm Optimization (PSO) algorithm, rather than being directly computed from CFD results. In recent years, heuristic algorithms have seen increasing use in CFD and design optimization due to their cost efficiency and ability to explore wide parameter ranges that would be challenging with conventional methods.

This work focuses on non-premixed hydrogen-air combustion devices. Non-premixed combustion of hydrogen can result in high NO_x production due to the locally high temperatures reached in the combustion chamber. However, this combustion mode mitigates the risk of accidents due to flashback, which is a concern in premixed combustion, as extensively studied in literature [30–33]. Therefore, non-premixed combustion reduces safety concerns in system design.

The objectives of this study are the following:

- Demonstrate the effectiveness of steam injection in reducing NO_x emissions in non-premixed hydrogen/air combustion.
- Propose a CRN capable of predicting NO_x emissions in a non-premixed lab burner.
- Evaluate the CRN's predictive capability beyond the conditions for which it was optimized, through comparisons with CFD simulations.

To the best of the authors' knowledge, this is the first study to propose the use of an optimization algorithm for the proper dimensioning of chemical reactor networks, in particular in the context of non-premixed combustion. The paper is structured as follows: a brief overview of the experimental setup will be presented in Section 2, followed by a discussion of the numerical methods in Section 3. Results from 1D counterflow simulations, CFD, and the CRN will be presented and analyzed in Section 4, while the key findings will be concisely summarized in Section 5.

2. Experimental setup

The experimental campaign was conducted at the Combustion and Optical Diagnostic Laboratory of Politecnico di Milano, utilizing a laboratory-scale, non-premixed swirl burner operating under ambient pressure. Detailed descriptions of the experimental setup and results are available in [34], while a schematic of the burner geometry is presented in Fig. 1. Here, only the most relevant information are summarized.

The swirl burner consists of two coaxial tubes: the central tube delivers the fuel, while swirling airflow is introduced through the surrounding annulus. The inner and outer radii of the annular air passage are $R_i = 7.5$ mm and $R_b = 18$ mm, respectively. Fuel is injected axially through a single-hole nozzle with an inner diameter of $d = 8$ mm, positioned precisely at the burner throat. The swirling motion of air is generated through a combination of axial and tangential air inlets, and the swirl intensity is adjusted by varying the relative contributions of these flows. The flame is confined within a cylindrical quartz chamber with an internal diameter of 192 mm and a length of 300 mm, which provides optical access. Exhaust gases exit through a conical hood with a 4:1 area contraction, positioned above the quartz cylinder. A stainless-steel probe, mounted on a cylindrical extension of the hood, is used to sample the exhaust gases for nitrogen oxides and oxygen analysis. Nitrogen oxides (NO and NO_2) are measured using a chemiluminescence-based technique, which relies on the gas-phase reaction between O_3 and NO. The sampled gas is first passed through a NO_2-to-NO converter, which reduces NO_2 to NO, allowing the total NO_x concentration to be determined. Oxygen concentration is measured using a paramagnetic-based technique. All pollutant measurements are reported on a dry basis. The gas analyzer was calibrated using certified reference gases, and the standard deviation of the measured NO_x concentrations was approximately 4% of the mean value. Measurements

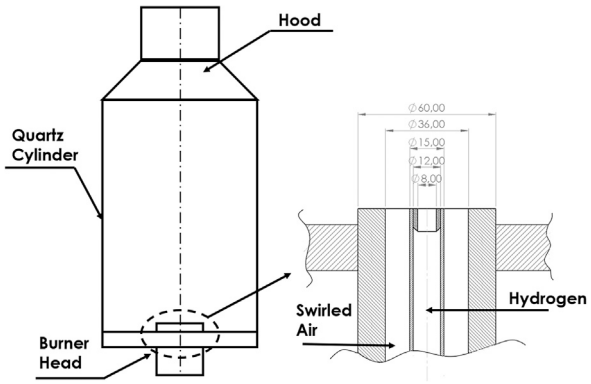

Fig. 1. Schematic of the burner geometry. Dimensions are in mm.

were performed at a swirl number $S = 1.0$ and an air Reynolds number $Re_{air} = 20150$. The swirl number was calculated using the simplified definition provided by [35], which neglects static pressure and velocity fluctuations. This computation was based on the mean axial ($\bar{v}_x$) and tangential ($\bar{v}_\theta$) velocity profiles measured via Laser Doppler Velocimetry (LDV) 1 mm downstream of the burner exit under isothermal conditions:

$$S = \frac{\int_0^{R_b} r^2 \bar{v}_x \bar{v}_\theta dr}{R_b \int_0^{R_b} r \bar{v}_x^2 dr} \tag{2}$$

where R_b represents the outer radius of the annular air passage and r is the radial coordinate. The hydrogen mass flow rate was set to approximately 0.048 g/s (equivalent to 32 Nl/min), corresponding to an input thermal power of 5.8 kW, and the global equivalence ratio was set at $\phi = 0.17$. The fuel jet Reynolds number, calculated at 300 K and based on the 8 mm nozzle diameter, was approximately $Re_{fuel} \simeq 770$. NO_x emissions, reported in terms of NO_x dry ppm referenced at 3% of oxygen, are equal to 70 ppm.

3. Numerical methods

3.1. Counter-flow diffusion flame

In the present study, we begin by analyzing emissions in the canonical configuration of a counter-flow diffusion flame, to demonstrate in an academic configuration the ability of steam to reduce emissions. In this configuration, the oxidizer and fuel streams are positioned directly opposite each other, converging in the central region. The initially unmixed streams generate a central mixing zone where combustion occurs under near-stoichiometric conditions. The subsequent evolution of the flame tends toward a steady-state solution, which is computed using the Cantera software [36], in which the equations described by Kee et al. [37] are solved.

Boundary conditions must be established at both inlets, as they significantly influence the flame's behavior and structure. The imposed quantities include mass flow rate, temperature, composition of the two inflows, and the distance between them, while the pressure remains constant throughout the one-dimensional domain. Subsequently, the flow strain is determined, critically affecting the flame structure, transitioning from equilibrium conditions in the limiting case of no strain to perfect mixing in the case of infinite strain, while also addressing flame quenching. In practical applications, varying levels of strain exist within the burner. Since strain is a fundamental parameter influencing flame structure, different strain rates have been investigated to capture these variations.

The approach employed for this series of one-dimensional simulations follows that proposed by Fiala and Sattelmayer [38]. The premise is that for different strain rate levels, if the distance and inlet velocity are appropriately modified, the thermochemical fields can be mapped from a solution at a different strain rate (i.e. a solution obtained in a previous simulation). The velocity and distance must satisfy the following relations:

$$v_{x,new} = v_{x,old} \left(\frac{a_{new}}{a_{old}} \right)^{1/2} ; \quad d_{new} = d_{old} \left(\frac{a_{new}}{a_{old}} \right)^{-1/2} \tag{3}$$

In this equation, a represents the strain rate, while v_x and d denote inlet velocities and distance, respectively. The subscript *old* and *new* refers to quantities related to the previous or the actual conditions. This method enables the mapping of solutions obtained from previous strain rate levels, necessitating only a few iterations to achieve accurate results. It has been demonstrated that simulating different counter-flow flames at varying strain rates is significantly faster with this approach compared to using other initial guesses [38].

3.2. Computational fluid dynamics - CFD

The CFD simulations are performed in Ansys® Fluent with 2D swirl axisymmetric RANS. This formulation neglects every derivative along the θ direction while accounting for a tangential component of velocity v_θ variable along x and r directions. The analysis takes into account variable density using Favre-averaged variables, denoted by a tilde, for a generic scalar ϕ,

$$\tilde{\phi} = \frac{\overline{\rho\phi}}{\bar{\rho}} \tag{4}$$

where the overbar indicates the typical Reynolds averaging and ρ represents the density. The resulting compressible 2D RANS equations can be written in cylindrical coordinates [39, 40]:

$$\frac{\partial \bar{\rho}}{\partial t} + \frac{1}{r}\frac{\partial}{\partial x}\left(\bar{\rho} r \tilde{v}_x\right) + \frac{\partial}{\partial r}\left(\bar{\rho}\tilde{v}_r\right) + \bar{\rho}\frac{\tilde{v}_r}{r} = 0 \tag{5}$$

$$\frac{\partial}{\partial t}\left(\bar{\rho}\tilde{v}_x\right) + \frac{1}{r}\frac{\partial}{\partial x}\left(r\bar{\rho}\tilde{v}_x\tilde{v}_x\right) + \frac{1}{r}\frac{\partial}{\partial r}\left(r\bar{\rho}\tilde{v}_r\tilde{v}_x\right) = -\frac{\partial \bar{p}}{\partial x} + \frac{1}{r}\frac{\partial}{\partial x}\left(r\hat{\tau}_{xx}\right) + \frac{1}{r}\frac{\partial}{\partial r}\left(r\hat{\tau}_{rx}\right) \tag{6}$$

$$\frac{\partial}{\partial t}\left(\bar{\rho}\tilde{v}_r\right) + \frac{1}{r}\frac{\partial}{\partial x}\left(r\bar{\rho}\tilde{v}_x\tilde{v}_r\right) + \frac{1}{r}\frac{\partial}{\partial r}\left(r\bar{\rho}\tilde{v}_r\tilde{v}_r\right) = -\frac{\partial p}{\partial r} + \frac{1}{r}\frac{\partial}{\partial x}\left(r\hat{\tau}_{xr}\right) + \frac{1}{r}\frac{\partial}{\partial r}\left(r\hat{\tau}_{rr}\right) + \frac{1}{r}\hat{\tau}_{rr} - \frac{1}{r}\hat{\tau}_{\theta\theta} + \bar{\rho}\frac{\tilde{v}_\theta^2}{r} \tag{7}$$

$$\frac{\partial}{\partial t}\left(\bar{\rho}\tilde{v}_\theta\right) + \frac{1}{r}\frac{\partial}{\partial x}\left(r\bar{\rho}\tilde{v}_x\tilde{v}_\theta\right) + \frac{1}{r}\frac{\partial}{\partial r}\left(r\bar{\rho}\tilde{v}_r\tilde{v}_\theta\right) = \frac{1}{r}\frac{\partial}{\partial x}\left(r\hat{\tau}_{x\theta}\right) + \frac{1}{r}\frac{\partial}{\partial r}\left(r\hat{\tau}_{r\theta}\right) + \frac{1}{r}\hat{\tau}_{r\theta} - \bar{\rho}\frac{\tilde{v}_r\tilde{v}_\theta}{r} \tag{8}$$

In these equations $\vec{v} = [v_x, v_r, v_\theta]$ represents the velocity vector with axial, radial, and tangential components. The variable r represents the radius, p represents the pressure and $\hat{\tau}$ represents the total stress tensor. The total stress tensor is a sum of the viscous and turbulent stress tensors, and its components are:

$$\hat{\tau}_{xx} = \left(\mu + \mu_t\right)\left(2\frac{\partial \tilde{v}_x}{\partial x} - \frac{2}{3}\nabla\cdot\vec{\tilde{v}}\right) - \frac{2}{3}\bar{\rho}\kappa \tag{9}$$

$$\hat{\tau}_{rr} = \left(\mu + \mu_t\right)\left(2\frac{\partial \tilde{v}_r}{\partial r} - \frac{2}{3}\nabla\cdot\vec{\tilde{v}}\right) - \frac{2}{3}\bar{\rho}\kappa \tag{10}$$

$$\hat{\tau}_{\theta\theta} = \left(\mu + \mu_t\right)\left(2\frac{\tilde{v}_r}{r} - \frac{2}{3}\nabla\cdot\vec{\tilde{v}}\right) - \frac{2}{3}\bar{\rho}\kappa \tag{11}$$

$$\hat{\tau}_{xr} = \left(\mu + \mu_t\right)\left(\frac{\partial \tilde{v}_x}{\partial r} + \frac{\partial \tilde{v}_r}{\partial x}\right) \tag{12}$$

$$\hat{\tau}_{x\theta} = \left(\mu + \mu_t\right)\left(\frac{\partial \tilde{v}_\theta}{\partial x}\right) \tag{13}$$

$$\hat{\tau}_{r\theta} = \left(\mu + \mu_t\right)\left(\frac{\partial \tilde{v}_\theta}{\partial r} - \frac{\tilde{v}_\theta}{r}\right) \tag{14}$$

with the divergence of the velocity field that in 2D axisymmetric condition is expressed as:

$$\nabla \cdot \vec{\tilde{v}} = \frac{\partial \tilde{v}_x}{\partial x} + \frac{\partial \tilde{v}_r}{\partial r} + \frac{\tilde{v}_r}{r} \tag{15}$$

The turbulent viscosity μ_t is calculated using the κ-ω Shear Stress Transport (SST) turbulence model [41], thus transporting the turbulence kinetic energy κ and the specific dissipation rate ω.

As the transport of species in the flow domain is considered, the energy equation contains, on top of the terms accounting for energy transfer due to conduction A and viscous dissipation B, a term accounting for the diffusion of the enthalpy of the species C and a term accounting for the heat generation from chemical reactions Ω. In 2D axisymmetric RANS, the energy equation is thus written as:

$$\frac{\partial}{\partial t}\left(\bar{\rho}\tilde{E}\right) + \frac{1}{r}\frac{\partial}{\partial x}\left(\bar{\rho} r \tilde{H} \tilde{v}_x\right) + \frac{1}{r}\frac{\partial}{\partial r}\left(\bar{\rho} r \tilde{H} \tilde{v}_r\right) = \frac{1}{r}\left(-A + B - C\right) + \Omega \tag{16}$$

with:

$$A = \frac{\partial}{\partial r}\left(r\, k_{eff}\frac{\partial \tilde{T}}{\partial r}\right) + \frac{\partial}{\partial x}\left(r\, k_{eff}\frac{\partial \tilde{T}}{\partial x}\right) \tag{17}$$

$$B = \frac{\partial}{\partial x}\left(r\left(\hat{\tau}_{xx}\tilde{v}_x + \hat{\tau}_{xr}\tilde{v}_r + \hat{\tau}_{x\theta}\tilde{v}_\theta\right)\right) + \frac{\partial}{\partial r}\left(r\left(\hat{\tau}_{xr}\tilde{v}_x + \hat{\tau}_{rr}\tilde{v}_r + \hat{\tau}_{r\theta}\tilde{v}_\theta\right)\right) \tag{18}$$

$$C = \frac{\partial}{\partial x}\left(r\sum_j \tilde{h}_j \vec{J}_j \cdot \vec{x}\right) + \frac{\partial}{\partial r}\left(r\sum_j \tilde{h}_j \vec{J}_j \cdot \vec{r}\right) \tag{19}$$

$$\Omega = -\sum_j \frac{h_j^0}{\mathcal{M}_j}\mathcal{R}_j \tag{20}$$

where E is the sum of internal and kinetic energy, $\vec{J}_j$ is the diffusion flux of species j, k_{eff} is the effective thermal conductivity and h_j^0, $\mathcal{M}_j$ and $\mathcal{R}_j$ are the enthalpy of formation, the molecular weight and the volumetric rate of formation, respectively, of the jth species. The effective thermal conductivity k_{eff} is defined as:

$$k_{eff} = k + \frac{c_p \mu_t}{Pr_t} \tag{21}$$

where c_p is the specific heat capacity at constant pressure and Pr_t is the turbulent Prandtl number. In this work, Pr_t was selected to be 0.85 and the c_p is obtained as the mixture-average of the c_p of all the species in the mixture. The molar heat capacity at constant pressure $\hat{c}_{p,j}$ is approximated by NASA7 polynomials [42] for the single species j, i.e.:

$$\frac{\hat{c}_{p,j}(T)}{R} = a_{0,j} + a_{1,j}T + a_{2,j}T^2 + a_{3,j}T^3 + a_{4,j}T^4 \tag{22}$$

with R being the universal gas constant. Thus, the specific sensible enthalpy for the single species j in the case of ideal gas approximation is calculated as:

$$\tilde{h}_j = \int_{T_{ref}}^{T} c_{p,j}\, d\tilde{T} \tag{23}$$

with T_{ref} being 298.15 K. Then, the specific sensible enthalpy of the mixture is evaluated as:

$$\tilde{h} = \sum_j \tilde{Y}_j \tilde{h}_j \tag{24}$$

and thus the variable $\tilde{H}$ represents:

$$\tilde{H} = \tilde{h} + \frac{\tilde{v}^2}{2} \tag{25}$$

The diffusion flux of species j is defined as:

$$\vec{J}_j = -\frac{1}{r}\left[\left(\rho D_{j,m} + \frac{\mu_t}{Sc_t}\right)\left(\frac{\partial\left(r\tilde{Y}_j\right)}{\partial r}\hat{r} + \frac{\partial\left(r\tilde{Y}_j\right)}{\partial x}\hat{x}\right) + \frac{D_{T,j}}{\tilde{T}}\left(\frac{\partial\left(r\tilde{T}\right)}{\partial r}\vec{r} + \frac{\partial\left(r\tilde{T}\right)}{\partial x}\vec{x}\right)\right] \tag{26}$$

where Sc_t is the turbulent Schmidt number, equal to 0.7, Y is the mass fraction, $D_{j,m}$ is the molecular mass diffusion coefficient and $D_{T,j}$ is the Soret diffusion coefficient. The unit vectors $\vec{x}$ and $\vec{r}$ denote the axial and radial directions, respectively.

A conservation equation is considered for $M-1$ species, where M denotes the total number of species in the mixture. The mass fraction of the excluded species is calculated as 1 minus the sum of the mass fractions of all the other species. To minimize the numerical error, N_2 is chosen to be the species not directly transported in the flow domain, as it is expected to have the largest mass fraction. These conservation equations are then written as:

$$\frac{\partial\left(\bar{\rho}\tilde{Y}_j\right)}{\partial t} + \frac{1}{r}\frac{\partial\left(r\bar{\rho}\tilde{v}_x\tilde{Y}_j\right)}{\partial x} + \frac{1}{r}\frac{\partial\left(r\bar{\rho}\tilde{v}_r\tilde{Y}_j\right)}{\partial r} = -\frac{1}{r}\left[\frac{\partial}{\partial x}\left(r\,\vec{J}_j \cdot \vec{x}\right) + \frac{\partial}{\partial r}\left(r\,\vec{J}_j \cdot \vec{r}\right)\right] + \mathcal{R}_j \tag{27}$$

The reaction rates $\mathcal{R}_j$ are modeled using the Eddy-Dissipation Concept (EDC) [43]. The EDC model assumes that the reactions only occur in the fine scales, i.e. in the smallest turbulence scales. It is then necessary to calculate the volume of the computational cell that is occupied by these fine scales, i.e. the volume fraction κ_{fs}:

$$\kappa_{fs} = \frac{\xi^2}{1-\xi^2} \tag{28}$$

In Eq. (28) the variable ξ represents the fine-structure region mass fraction, which is calculated as:

$$\xi = C_\xi\left(\frac{\nu\epsilon}{k^2}\right)^{\frac{1}{4}} \tag{29}$$

where C_ξ is a constant value equal to 2.1377, ν is the kinematic viscosity, κ is the turbulent kinetic energy and ϵ is the rate of dissipation of turbulent kinetic energy. Moreover, the reactions are integrated over the time scale τ^*, which is defined as:

$$\tau^* = C_\tau\left(\frac{\nu}{\epsilon}\right)^{\frac{1}{2}} \tag{30}$$

where C_τ is a constant value equal to 0.4082. Finally, the reaction rates $\mathcal{R}_j$ can be written as:

$$\mathcal{R}_j = \rho\kappa_{fs}\frac{Y_j^* - \tilde{Y}_j}{\tau^*} \tag{31}$$

where Y_j^* represents the fine-scale species mass fraction after reacting over the time scale τ^* in an adiabatic and isobaric perfectly stirred reactor, whose initial conditions are the species and temperature at the end of the previous time-step. Furthermore, the Fluent implementation of the Eddy Dissipation Concept (EDC) differs from the original formulation proposed by Magnussen et al. [44], as it does not account for the possibility that reactions may occur only within a fraction of the fine scales, among other modifications [45].

Moreover, the CFD domain is represented in Fig. 2: the air and hydrogen pipes are not included in the CFD simulation. Thus, a user-defined function (UDF) is employed at the air inlet to model the swirl velocity profile as a function of the radial coordinate r and the outer radius of the annular air passage R_b, derived from the definition of the swirl number:

$$\frac{v_\theta}{v_x} = \frac{R_b}{r} \tag{32}$$

This approach ensures a swirl number of 1 at the air inlet, consistent with the experimental measurements.

Finally, the simulations are carried out in Fluent using the pressure-based solver with the coupled algorithm for the pressure-velocity coupling [40]. The pressure values at the faces of the mesh are interpolated using the PRESTO! scheme [46], while the other quantities

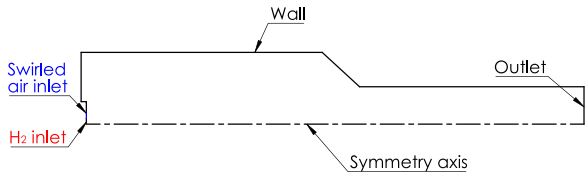

Fig. 2. CFD domain. The walls are adiabatic.

Table 1
Spatial discretization used for all the CFD simulations.

Quantity	Spatial discretization
Pressure	PRESTO!
Density	Third-Order MUSCL
Momentum	Third-Order MUSCL
Swirl Velocity	Third-Order MUSCL
Turbulent Kinetic Energy	Second Order Upwind
Specific Dissipation Rate	Second Order Upwind
Species	Third-Order MUSCL
Energy	Third-Order MUSCL

are discretized with second-order Upwind [47] or third-order MUSCL schemes [48]. The spatial discretization schemes adopted for each quantity and all CFD simulations are summarized in Table 1. Moreover, gradient evaluation is performed using the least squares cell-based method [40]. Similar settings have been investigated in the literature for the simulation of swirled flows [49, 50].

3.3. Chemical reactor network - CRN

The reactor network simulations are carried out using the Cantera library [36]. The single reactors are modeled as ideal gas perfectly stirred reactors (PSRs), considering adiabatic walls and constant volume reactors. The rate of change of mass inside the single reactors is accounted for by the net balance between all the inflow and outflow mass flow rates:

$$\frac{dm}{dt} = \sum_{in} \dot{m}_{in} - \sum_{out} \dot{m}_{out} \tag{33}$$

where m represents the mass inside the reactor and $\dot{m}$ the mass flow rate. The mass fraction Y_j of the jth species inside the reactor changes due to the transport of species j from the inflows and due to the generation or destruction in volumetric reactions:

$$m\frac{dY_j}{dt} = \sum_{in} \dot{m}_{in}\left(Y_{j,in} - Y_j\right) + \dot{m}_{j,gen} \tag{34}$$

$$\dot{m}_{j,gen} = V\mathcal{R}_j\mathcal{M}_j \tag{35}$$

where V is the volume, $\mathcal{M}_j$ is the molecular weight, and $\mathcal{R}_j$ is the net reaction rate of species j, which in the CRN model is calculated with the direct use of finite-rate kinetics. Finally, the temperature is calculated using the following equation:

$$mc_v\frac{dT}{dt} = \sum_{in} \dot{m}_{in}\left(h_{in} - \sum_j e_j\, Y_{j,in}\right) + - \frac{pV}{m}\sum_{out} \dot{m}_{out} - \sum_j \dot{m}_{j,gen}\, u_j \tag{36}$$

where c_v is the specific heat at constant volume, p is the pressure and e is the total specific internal energy.

The structure of the CRN proposed in this work is illustrated in Fig. 3. The PSR 1 represents the hydrogen jet emerging from the hydrogen inlet, while PSR 2 corresponds to the flame front in the mixing zone between the hydrogen jet and the swirled air. PSR 3 and PSR 5 denote the outer and inner recirculation zones, respectively, while PSR 4 represents the flame downstream of the hydrogen jet, and PSR 6 marks the combustor outlet.

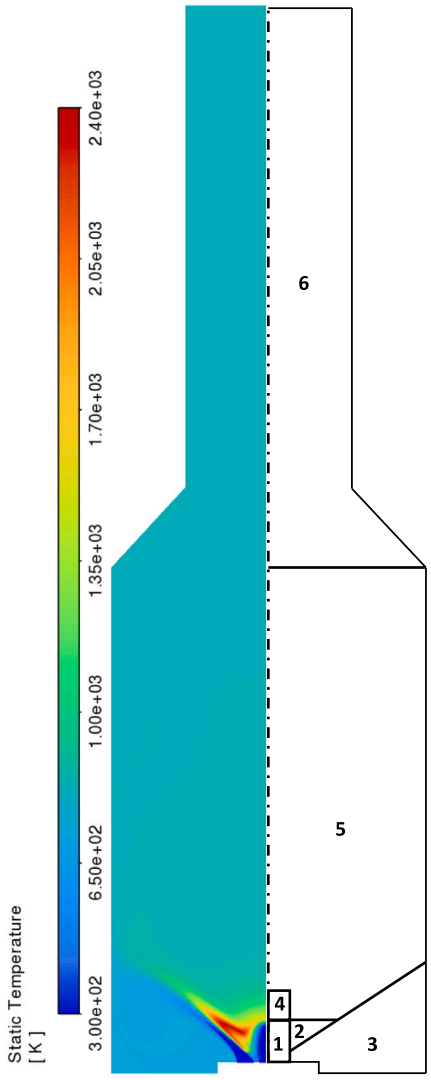

Fig. 3. The left panel displays a static temperature contour within the combustor, obtained from an axisymmetric 2D CFD simulation. The right panel illustrates the reactor network model, where each numbered region (1-6) represents a Perfectly Stirred Reactor (PSR) used to approximate the corresponding physical region.

These zones have been defined on the basis of physical considerations such as the presence of the hydrogen jet, the flame in the shear layer between hydrogen and air, and the recirculation zones induced by swirl. Their volumes have been estimated accordingly, using geometric approximations based on combustor geometry and flow physics principles. The CFD static temperature contour shown in Fig. 3 serves a specific purpose: it was used to assess the general flow structure and to extract the penetration length of the hydrogen jet, which is necessary to define the volume of PSR 1 and consequently PSR 2. It is important to note that, as will be discussed in Section 3.4, the optimization algorithm used to train the reactor network requires a scalar output to track, i.e. the experimental measurement of NO_x at the outlet of the burner in this work. Consequently, high-fidelity data, whether from CFD simulations or experiments, are always necessary before constructing the CRN. This ensures that at least some degree of information about the flow domain is available to approximate the reactors. The optimization procedure adjusts the network connections based on CFD or experimental data, ultimately determining well-suited residence times for the approximated volumes.

The volume of PSR 1 is defined as the product of the inlet area and the penetration length of the hydrogen jet. PSR 3 is approximated as

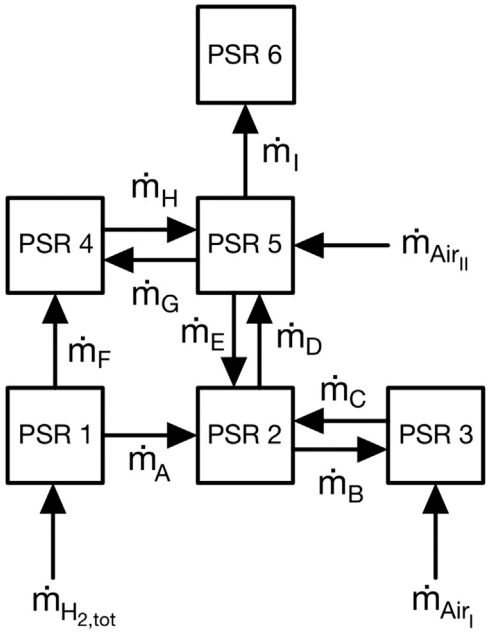

Fig. 4. CRN topology. Arrows indicate mass flow rates between reactors. The reactor numbers refer to the volumes highlighted in Fig. 3.

a cylinder minus a cone, whose opening angle is determined by the ratio of axial to swirl velocity, as described by the swirl number. PSR 2 is modeled as a truncated cone with the volume of PSR 1 subtracted. Its opening angle matches that of PSR 3, with an additional length included to account for the delayed onset of the flame. The volume of PSR 4 is approximated as half that of PSR 1. PSR 6 corresponds to the combustor volume downstream of the converging nozzle, while PSR 5 is determined as the total combustor volume minus the sum of all other reactor volumes. The reactor network topology is illustrated in Fig. 4, where the arrows indicate the mass flow rates that connect the different reactors.

Although some CRN connections can be derived analytically from the continuity equation, others are not uniquely defined and must be tuned to match the experimental result. This tuning is achieved using optimization algorithms, as detailed in Section 3.4, by varying the following four parameters:

$$\mathcal{P}_1 = \frac{\dot{m}_{Air_I}}{\dot{m}_{Air_{II}}} \tag{37}$$

$$\mathcal{P}_2 = \frac{\dot{m}_B}{\dot{m}_{Air_I}} \tag{38}$$

$$\mathcal{P}_3 = \frac{\dot{m}_F}{\dot{m}_A} \tag{39}$$

$$\mathcal{P}_4 = \frac{\dot{m}_G}{\dot{m}_I} \tag{40}$$

These four variables represent the degrees of freedom in our model and are determined based on experimental reference values, maintaining the same connections even with water injection. The total mass flow rate of hydrogen, $\dot{m}_{H_{2,tot}}$, enters in the PSR 1 while the total air mass flow rate, $\dot{m}_{Air_{tot}}$, is divided between two streams: $\dot{m}_{Air_I}$ entering PSR 3 and $\dot{m}_{Air_{II}}$ entering PSR 5. Together, these parameters constitute the optimized set $\mathcal{P}^{opt}$:

$$\mathcal{P}^{opt} = \left[\mathcal{P}_1, \mathcal{P}_2, \mathcal{P}_3, \mathcal{P}_4\right] \tag{41}$$

The mass flow rates are thus derived in the following way:

$$\dot{m}_{Air_I} = \frac{\mathcal{P}_1}{\mathcal{P}_1 + 1} \cdot \dot{m}_{Air_{tot}} \tag{42}$$

$$\dot{m}_{Air_{II}} = \dot{m}_{Air_{tot}} - \dot{m}_{Air_I} \tag{43}$$

$$\dot{m}_A = \frac{\dot{m}_{H_{2,tot}}}{1 + \mathcal{P}_3} \tag{44}$$

$$\dot{m}_B = \mathcal{P}_3 \cdot \dot{m}_{Air_I} \tag{45}$$

$$\dot{m}_C = \frac{\dot{m}_{Air_I}}{1 + \mathcal{P}_2} \tag{46}$$

$$\dot{m}_D = \dot{m}_A + \dot{m}_C + \dot{m}_E - \dot{m}_B \tag{47}$$

$$\dot{m}_F = \mathcal{P}_3 \cdot \dot{m}_A \tag{48}$$

$$\dot{m}_G = \mathcal{P}_4 \cdot \dot{m}_I \tag{49}$$

$$\dot{m}_H = \dot{m}_E + \dot{m}_G + \dot{m}_I - \dot{m}_D - \dot{m}_{Air_{II}} \tag{50}$$

$$\dot{m}_I = \dot{m}_{Air_{tot}} + \dot{m}_{H_{2,tot}} \tag{51}$$

Furthermore, the mass flow rate $\dot{m}_E$ has not yet been defined. This value is determined through a control mechanism that ensures PSR 2 approaches the stoichiometric equivalence ratio. Specifically, ϕ_{PSR2} is set to 1 if the inlet conditions allow, or otherwise, it is assigned the highest possible equivalence ratio between 0 and 1, aiming to replicate the stoichiometric flame front characteristic of a non-premixed flame. Thus, $\dot{m}_E$ is computed as:

$$K_1 = \dot{m}_A \cdot Y_{H2}^{PSR1} - (\dot{m}_B + \dot{m}_D) \cdot Y_{H2}^{PSR2}$$

$$K_2 = \dot{m}_A \cdot Y_{O2}^{PSR1} + \dot{m}_C \cdot Y_{O2}^{PSR3} - (\dot{m}_B + \dot{m}_D) \cdot Y_{O2}^{PSR2}$$

$$\dot{m}_E = \frac{K_1 - f_{st}^{H_2-O_2} \cdot K_2}{f_{st}^{H_2-O_2} \cdot Y_{O2}^{PSR5} - Y_{H2}^{PSR5}} \tag{52}$$

where $f_{st}^{H_2-O_2}$ is the stoichiometric fuel-to-air ratio of hydrogen and oxygen. Whenever the check is performed and consequently the flow rate $\dot{m}_E$ changes, the flow rates $\dot{m}_D$ and $\dot{m}_H$ are also changed accordingly to ensure the continuity of the mass in the reactors as in Eqs. (47) and (50).

3.4. Optimization

In this study, the fluxes between different 0D reactors were computed using an evolutionary optimization algorithm. In particular, a Particle Swarm Optimization (PSO) algorithm was selected [51]. The PSO algorithm is inspired by the social behavior of flocks of birds and schools of fish searching for food. Unlike Genetic Algorithms (GAs), the PSO algorithm does not require the tuning of operators. Instead, it models candidate solutions as particles that fly through the solution space, guided by their own best-known positions and the best position discovered by the whole swarm. Each particle's motion is influenced by three components: inertia w, cognitive acceleration, and social acceleration. The cognitive acceleration c_1 attracts a particle toward its personal best position $p_{k,best}$, while the social term c_2 attracts it toward the global best position g_{best} found by the swarm. Particle velocities are updated at each iteration as follows:

$$v_k = w \cdot v_k + c_1 \cdot r_1 \cdot (p_{k,\text{best}} - p_k) + c_2 \cdot r_2 \cdot (g_{\text{best}} - p_k) \tag{53}$$

where r_1 and r_2 are random numbers used to introduce stochasticity, and p_k is the position of the kth particle.

The PSO algorithm often converges more rapidly to global optima compared to GAs due to its efficient information-sharing mechanism [52]. Additionally, this study incorporated the improvements proposed by Trelea [53], which may involve variable inertia and

Table 2
Equivalence ratio needed for each water mass fraction to keep a constant outlet temperature. The equivalence ratio is based on the Bilger mixture fraction, including the water mass fraction in the oxidizer composition.

Y_{H_2O}	ϕ
0%	0.170
5%	0.187
10%	0.206

acceleration coefficients over iterations. These modifications enhance the algorithm's performance by balancing exploration during the early stages and exploitation in later stages when promising solutions are found. One thousand generations are set with a swarm size of 10 individuals. In this work, the Trelea approach was applied only to the inertia weight, with initial value $w = 0.9$ and an end value of $w = 0.4$, while the cognitive acceleration, and social acceleration were kept constant to the values of $c_1 = 1.5$, $c_2 = 1.5$. These values are consistent with the ones present in the literature [52]. The fitness function used in this study quantifies the relative difference of NO_x emissions between the values predicted by the Chemical Reactor Network (CRN) and the experimental measurements [34]:

$$f = 1 - \left| \frac{NO_x^{CRN}}{NO_x^{exp}} \right| \tag{54}$$

Finally, the bounds for the solutions, here representing the ratios of mass fluxes between the reactors, are constrained between 0 and 1. These limits were determined based on the assumption that some fluxes must be larger than others, informed by observations of flow behavior. The five optimization parameters used in this study will be detailed in Section 4, where the results of the CRN optimization are presented.

3.5. Parameter selections

A series of parametric variations were conducted in the CFD and CRN simulations. The primary objective was to evaluate steam injection as a potential technique for reducing NO_x emissions. Steam loadings of 5% and 10% by mass were selected for injection into the combustion chamber alongside the airflow. Steam injection impacts the outlet temperature, which is a critical design parameter for the combustion chamber. Additionally, it influences NO_x production through thermal pathways. Since outlet temperature is a relevant design parameter, a control strategy was implemented to maintain it constant in the CFD and CRN simulations. This aim was achieved by increasing the equivalence ratio. The adopted approach is consistent with the method proposed by Concetti et al. [16]. Specifically, the strategy involves iteratively increasing the equivalence ratio until the adiabatic temperature for the case with steam injection matches the adiabatic temperature for the reference case without steam addition. The equivalence ratios needed are summarized in Table 2.

3.6. Chemical mechanisms

In this work, to guarantee that the methodology proposed is independent from the chemical description considered, three chemical mechanisms have been used: these are the Naik mechanism, available in Ansys® Fluent [54], the Reduced Gotama [55] and the Creck [56–58] mechanism. All of these mechanisms comprehend a detailed chemistry of nitrogen oxidation and they are summarized in Table 3.

These three mechanisms have been selected based on their widespread application and their established validation in the literature for nitrogen chemistry modeling. The Naik mechanism has been applied in gas turbine combustion studies [59, 60], and similarly, the Gotama mechanism has demonstrated successful implementation in this sector [61, 62]. Both mechanisms offer a balance between computational efficiency and chemical detail, making them particularly suitable for complex reacting flow simulations. The Creck mechanism provides the most comprehensive nitrogen oxidation chemistry among the three, as evidenced by its use in detailed pollutant formation studies [25, 63]. This selection ensures that the proposed methodology is validated across different levels of chemical complexity and computational requirements, demonstrating its robustness and general applicability.

4. Results

4.1. Counterflow flames

The results for counterflow diffusion flames are presented to illustrate flame behavior under steam injection in a configuration that, while idealized compared to actual burners, is straightforward to simulate and analyze. Diffusive flames are characterized by localized high temperatures due to the presence of stoichiometric reactant concentrations in the central part of the mixing region. Fig. 5 shows the maximum temperature of a counterflow diffusive flame as a function of the strain rate. The results are obtained using the chemical mechanism proposed by Song et al. [56], Stagni et al. [57,58], which accurately captures the high-temperature chemistry of hydrogen/air combustion as well as nitrogen chemistry. At low strain rates, the flame tends to approach chemical equilibrium conditions and a temperature of around 2300 K. However, as the strain rate increases, mixing is enhanced, leading to a decrease in the maximum temperature until a stable flame can no longer be sustained. The presence of water vapor further reduces the maximum flame temperature and decreases the strain rate at which flame quenching occurs. Due to the significance of the thermal pathway in NO_x formation, for the considered conditions, a reduction in these pollutants is expected when steam is added to the system. The maximum molar fraction of NO for the counterflow flame configuration is shown in Fig. 6. It can be noticed that NO abatement is most significant at low strain rates, while at high strain rate the NO concentration is anyway low. The observed trends in temperature and NO concentration with increasing water vapor content in the analyzed configuration suggest that steam injection could be a viable strategy for reducing NO_x emissions, without reducing extremely the maximum temperature reached by the system. The present results preliminarily confirm that steam addition can lead to a reduction in NO_x emissions also in a non-premixed flame configuration. However, the results presented here pertain only to the counterflow configuration, which does not closely represent realistic conditions in industrial burners and combustion chambers. In fact, even if the computational cost of steady-state counterflow simulations is generally negligible compared to CFD simulations, their quantitative validity remains uncertain. For this reason, in the following subsections, alternative strategies for assessing the potential of water injection in emissions abatement for combustion devices relevant to industrial applications are explored, starting from the promising findings of the present simplified study.

4.2. CFD

NO_x emissions are reported in terms of NO_x dry ppm, referenced at 3% of oxygen, following [34]. These values are calculated at the combustor outlet, and the ppm values are calculated as follows:

$$NO_{x,\,ppm,\,dry,\,3\%\,O_2} = \left(X_{NO} + X_{NO_2}\right) \cdot \left(\frac{X_{O_2,\,inlet} - X_{O_2,\,ref}}{X_{O_2,\,inlet} - X_{O_2}}\right) \cdot \frac{10^6}{1 - X_{H_2O}} \tag{55}$$

In Eq. (55) the symbol X denotes the mole fraction.

Thus, NO_x emissions are presented in Table 4 for a mesh of 350 000 cells and in Table 5 for a mesh of 1 400 000 cells. A further simulation

Table 3
Kinetic mechanisms used in both the CFD and CRN simulations.

Mechanism	# Species	List of species	# Reactions
Naik [54]	21	H, H_2, H_2O, H_2O_2, HNO, HO_2, HONO, $HONO_2$, N, N_2, N_2O, NH, NH_2, NH_3, NNH, NO, NO_2, O, O_2, OH	105
Reduced Gotama [55]	25	Ar, H, H_2, H_2NO, H_2NN, H_2O, H_2O_2, H_2O_2, HNO, He, N, N_2, N_2H_2, N_2H_3, N_2H_4, N_2O, NH, NH_2, NH_3, NNH, NO, NO_2, O, O_2, OH	110
Creck [56] [57, 58]	31	Ar, H, H_2, H_2NN, H_2O, H_2O_2, H_2OH, HNO, HNO_2, HNOH, HO_2, HONO, $HONO_2$, N, N_2, N_2H_2, N_2H_3, N_2H_4, N_2O, NH, NH_2, NH_2OH, NH_3, NNH, NO, NO_2, NO_3, O, O_2, OH	203

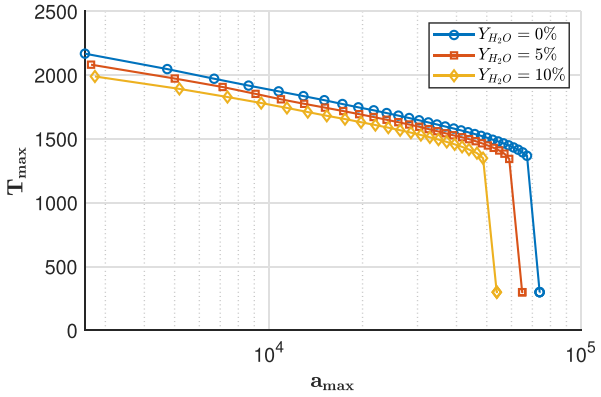

Fig. 5. Maximum temperature for different strain and mass fraction of injected steam for counterflow flames. The fast temperature decrease at a high level of strain rate represents the flame quenching.

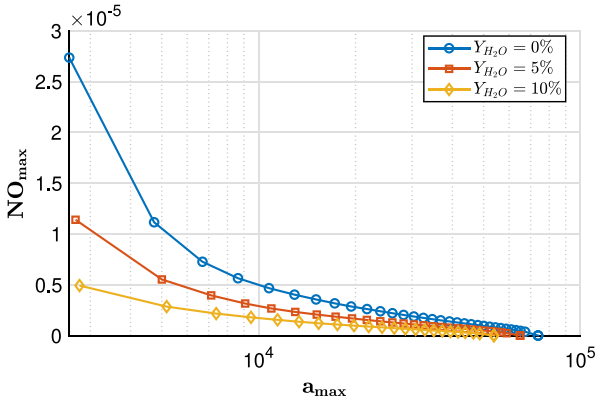

Fig. 6. Maximum NO molar fractions for different strain and water mass fraction for counterflow flames.

Table 4
NO_x production predicted by CFD under different chemical mechanisms and water loading. Values represent NO_x ppm at 3% O_2. Grid with 350,000 cells.

CFD	Naik	Gotama	Creck
$Y_{H_2O} = 0\%$	65.80	79.94	62.16
$Y_{H_2O} = 5\%$	21.56	28.21	18.05
$Y_{H_2O} = 10\%$	8.07	11.86	6.31

using 5 600 000 cells is performed with the Naik mechanism for a water loading of 0%, resulting in an emission of 74.91 dry ppm at 3% O_2, which is for our purposes sufficiently close to the value (i.e. 73.86) obtained on the medium mesh. These results suggest that the mesh with 1 400 000 is suitable for the simulation of this burner.

Table 5
NO_x production predicted by CFD under different chemical mechanisms and water loading. Values represent NO_x ppm at 3% O_2. Grid with 1400,000 cells.

CFD	Naik	Gotama	Creck
$Y_{H_2O} = 0\%$	73.86	83.61	68.00
$Y_{H_2O} = 5\%$	22.79	29.10	19.64
$Y_{H_2O} = 10\%$	8.32	12.05	6.40

The results indicate that, as expected, the Creck mechanism, being the largest reaction mechanism among those investigated, is the closest to the experimental result of 70 ppm. The Naik mechanism, although having the smallest number of species and reactions, is also close to the Creck mechanism and the experimental result. In contrast, the Gotama mechanism appears to provide the largest discrepancy with the experimental result. This discrepancy can be attributed to the fact that the Gotama mechanism was specifically optimized for accurately predicting laminar flame speeds of hydrogen-ammonia fuel blends rather than NO_x formation pathways [55]. Nevertheless, despite the quantitative overprediction, the Gotama mechanism correctly captures the same qualitative trends observed with the Naik and Creck mechanisms, particularly the significant reduction in NO_x formation with increasing water loading (from about 84 ppm at $Y_{H_2O} = 0\%$ to 12 ppm when $Y_{H_2O} = 10\%$), indicating that the underlying physics of the water addition on NO_x formation is represented. To further show grid convergence, the variations in temperature (Fig. 7), axial velocity (Fig. 8) and radial velocity (Fig. 9) are presented at an axial distance of 2 cm from the injector for the three different meshes. These results correspond to simulations performed using the Naik mechanism without water injection, i.e., $Y_{H_2O} = 0$ %. This location is chosen because it intersects the flame front, making it a particularly sensitive and challenging region for assessing numerical accuracy. The plots consistently show that the results obtained with the 1.4 million cell mesh and the 5.6 million cell mesh are nearly indistinguishable for all three variables, indicating that grid convergence has been achieved. Furthermore, the temperature (Fig. 10), axial velocity (Fig. 11), and radial velocity (Fig. 12) are shown as a function of radius at an axial location 2 cm from the inlet. This location is again selected because it intersects the flame region, making it suitable for comparing different reaction mechanisms. Additionally, a simulation with isothermal flow is included to highlight the effect of chemistry on the velocity field, which is affected by the presence of the flame. These graphs show that the Creck and Naik mechanisms are in close agreement, almost overlapping, while the Gotama mechanism displays small, but noticeable differences.

Furthermore, temperature contour plots for different water loadings are presented in Fig. 13(a), Fig. 13(b), and Fig. 13(c). These plots demonstrate that an outlet temperature of approximately 850 K can be maintained by appropriately increasing the equivalence ratio in response to higher water loading. They also highlight that water addition reduces both the peak and overall flame temperatures, despite the increased equivalence ratio. Specifically, for varying water loadings,

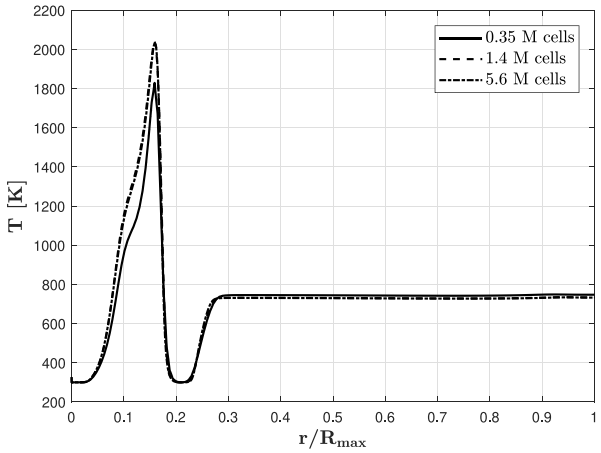

Fig. 7. Temperature variation across the radius r, normalized with the maximum radius of the chamber R_{max}, at an axial distance of 2 cm from the injector. Naik mechanism, $Y_{H_2O} = 0$ %.

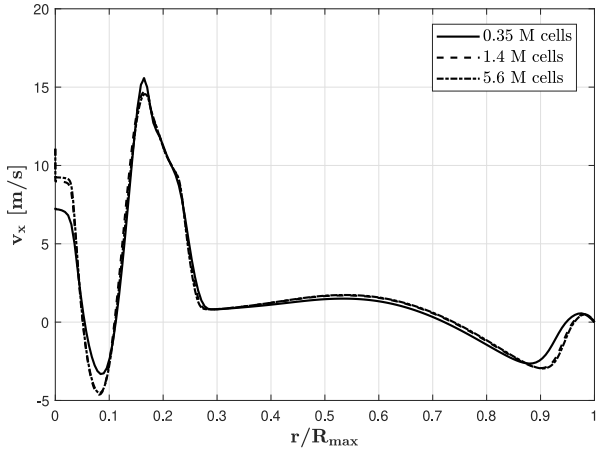

Fig. 8. Axial velocity variation across the radius r, normalized with the maximum radius of the chamber R_{max}, at an axial distance of 2 cm from the injector. Naik mechanism, $Y_{H_2O} = 0$ %.

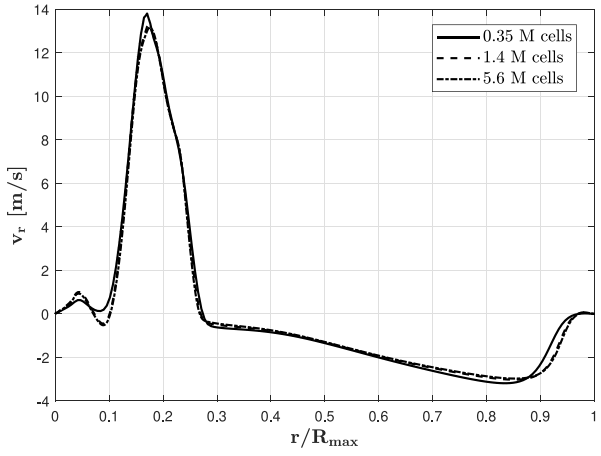

Fig. 9. Radial velocity variation across the radius r, normalized with the maximum radius of the chamber R_{max}, at an axial distance of 2 cm from the injector. Naik mechanism, $Y_{H_2O} = 0$ %.

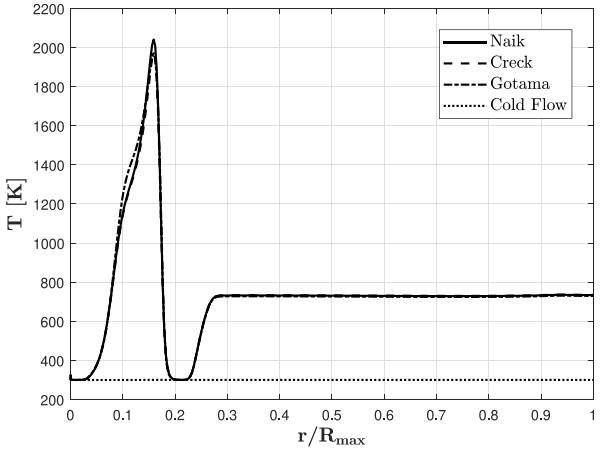

Fig. 10. Temperature variation across the radius r, normalized with the maximum radius of the chamber R_{max}, at an axial distance of 2 cm from the injector.

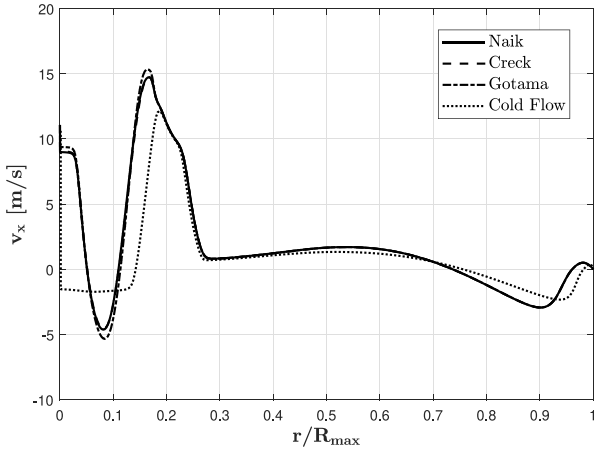

Fig. 11. Axial velocity variation across the radius r, normalized with the maximum radius of the chamber R_{max}, at an axial distance of 2 cm from the injector.

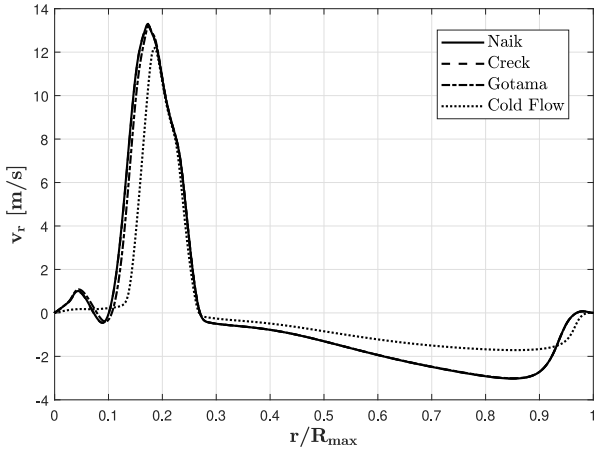

Fig. 12. Radial velocity variation across the radius r, normalized with the maximum radius of the chamber R_{max}, at an axial distance of 2 cm from the injector.

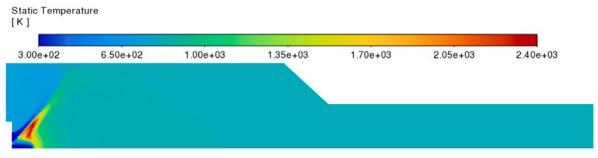

(a) Temperature contour plot using Naik mechanism in the case of $Y_{H_2O} = 0\%$.

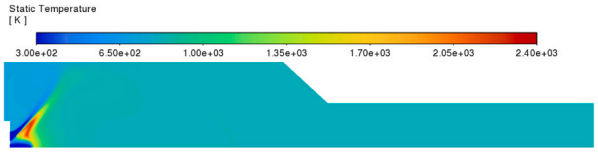

(b) Temperature contour plot using Naik mechanism in the case of $Y_{H_2O} = 5\%$.

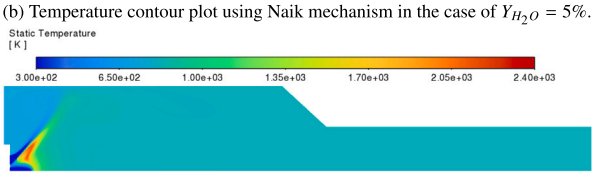

(c) Temperature contour plot using Naik mechanism in the case of $Y_{H_2O} = 10\%$.

Fig. 13. Temperature contour plots using Naik mechanism for different water loadings.

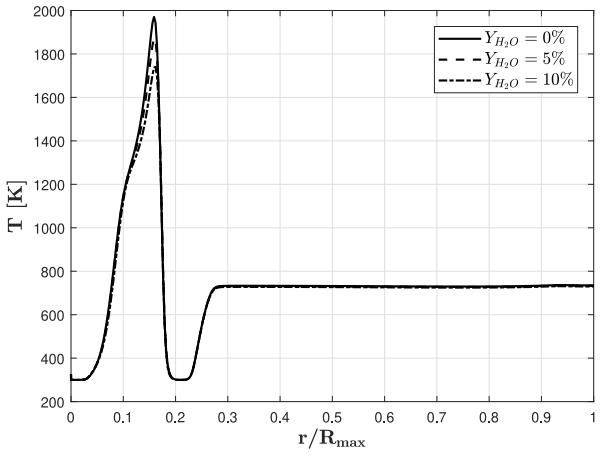

Fig. 14. Temperature variation across the radius r, normalized with the maximum radius of the chamber R_{max}, at an axial distance of 2 cm from the injector. Results are presented using Creck mechanism for different values of water mass fraction at the inlet.

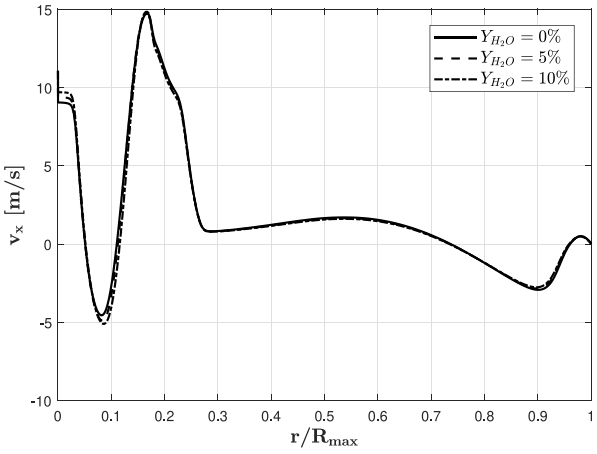

Fig. 15. Axial velocity variation across the radius r, normalized with the maximum radius of the chamber R_{max}, at an axial distance of 2 cm from the injector. Results are presented using Creck mechanism for different values of water mass fraction at the inlet.

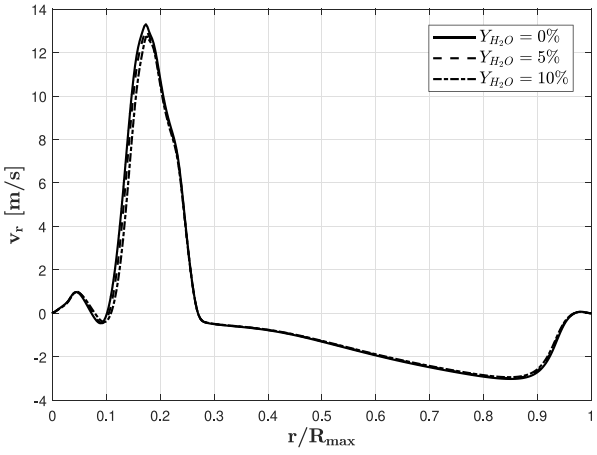

Fig. 16. Radial velocity variation across the radius r, normalized with the maximum radius of the chamber R_{max}, at an axial distance of 2 cm from the injector. Results are presented using Creck mechanism for different values of water mass fraction at the inlet.

the temperature (Fig. 14), axial velocity (Fig. 15), and radial velocity (Fig. 16) are depicted as a function of radius at an axial position of 2 cm from the inlet. These graphs illustrate the temperature reduction due to water injection and indicate that the velocity fields remain largely unaffected.

The validation of the CFD framework, whose results have been presented here, was carried out using emission data from a single experimental condition without water injection. However, the results presented on the effects of steam dilution align well with trends reported in the literature [64–67], thus supporting the physical validity of the CFD approach.

Finally, estimating the computational cost of a single CFD simulation is not straightforward, as each refined grid run was initialized using a flow field obtained previously. In addition, modifications such as the introduction of water loading or changes in the chemical mechanism were applied during restarts. This strategy significantly reduced the computational expense associated with more complex chemical mechanisms and finer meshes. However, to provide a general estimate, each simulation required approximately 10^3 CPU hours.

4.3. Chemical reactor network

The CRN is optimized for each chemical mechanism to match the experimentally observed NO_x levels without water injection. Specifically, the optimization is performed for the Naik mechanism, and the obtained solution is subsequently perturbed to derive solutions for the other two mechanisms. This approach can be applied to generate an optimal parameter set for more complex chemical mechanisms by starting with simpler ones. The parameters resulting from this procedure are presented in the following vectors:

$$\mathcal{P}^{opt}_{Naik} = [0.189;\ 0.125;\ 0.216;\ 0.099] \tag{56}$$

$$\mathcal{P}^{opt}_{Creck} = [0.172;\ 0.125;\ 0.216;\ 0.099] \tag{57}$$

$$\mathcal{P}^{opt}_{Gotama} = [0.217;\ 0.125;\ 0.216;\ 0.099] \tag{58}$$

These parameters define the connections between the reactors in both scenarios with and without water injection. Each mechanism requires a different set of connections. This is explained by the need for different residence times for the mechanisms to achieve the experimental result.

Table 6
Comparison of NO_x production for CRN under different chemical mechanisms and water loading. Values represent NO_x ppm dry at 3% O_2.

CRN	Naik	Gotama	Creck
$Y_{H_2O} = 0\%$	70.00	70.00	70.00
$Y_{H_2O} = 5\%$	28.60	35.02	21.47
$Y_{H_2O} = 10\%$	11.13	18.77	7.21

The NO_x levels (in ppm dry at 3% O_2) calculated using this procedure are presented in Table 6.

The results indicate that the optimization procedure successfully identifies an appropriate set of parameters for each reaction mechanism, allowing for the accurate reproduction of the experimental value of 70 ppm when no water is injected, showing that the optimization procedure can be performed successfully regardless of the reaction mechanism used. In addition, a comparison with the CFD results, as shown in Table 5, highlights the ability of the reactor network to assess the impact of gaseous water injection on NO_x emissions. In particular, the reduced Gotama mechanism exhibits the largest deviation from the CFD results, as expected, given that the CRN is calibrated to reproduce a NO_x level of 70 ppm, while the CFD with Gotama predicts an emission closer to 84 ppm. In contrast, the Creck mechanism shows the best agreement with the CFD data, in addition to being the closest to the experimental result in the CFD scenario. Fig. 17 provides a comparative visualization of these findings across the three chemical mechanisms, with blue bars representing the predictions of the reactor network and dark orange bars showing the corresponding CFD results. At the validation condition (0% water loading), the Creck, Naik, and Gotama mechanisms exhibit relative errors of 2.9%, 5.2%, and 16.3%, respectively, between CFD and CRN, corresponding to absolute errors, i.e. $NO_x^{CFD} - NO_x^{CRN}$, of −2.00, +3.86, and +13.61 ppm, respectively. Under water injection conditions, absolute errors evolve to −1.83, −5.81, and −5.92 ppm at 5% water loading, and −0.81, −2.81, and −6.72 ppm at 10% water loading for the Creck, Naik, and Gotama mechanisms, respectively. Importantly, the mechanism showing the best agreement at the validation condition, i.e. Creck, maintains the most consistent performance across all water injection scenarios, while the Gotama mechanism, which shows the largest deviation in the validation case, continues to exhibit less agreement under water injection conditions. The Naik mechanism shows an intermediate behavior between these two extremes. Although percentage errors generally increase with water loading due to the decreasing absolute NO_x levels, the relative ranking of mechanism performance remains consistent. This analysis suggests that the choice of chemical mechanism can be effectively guided by evaluating the CRN-CFD agreement at the validation condition, as this appears to be a reliable predictor of model consistency across different operating conditions.

All simulations converge to a stationary solution. An example of the progress of physical quantities within the CRN is shown in Fig. 18, where it is evident that the steady state is achieved, with both the static temperature and the NO_x ppm remaining constant over time.

Furthermore, a scheme of the reactor network showing the temperature T, pressure p, equivalence ratio ϕ and molar fractions for the different species is presented in Fig. 19, which is built using the Creck mechanism and considering a water loading of 0%. It is possible to see how, after the optimization, the reactor network follows the assumptions made in its realization, i.e. the maximum temperature is inside PSR 2, while tending to the stoichiometric equivalence ratio, ignition occurs in PSR 4 and in the last reactor the overall equivalence ratio is established. It is also important to highlight the computational cost of using the CRN, which includes both the cost associated with training the reactor network via the optimization procedure and the cost of running the simulation in Cantera. The former can be estimated at 0.5 CPU hours, on an average of 5 restarts with a random initial guess. The latter, however, is significantly faster, with a cost of approximately

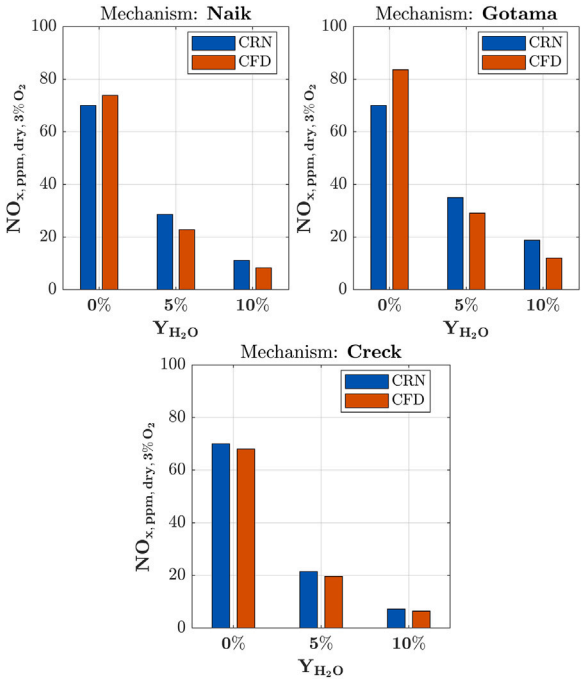

Fig. 17. Bar charts comparing the NO_x prediction for the three reaction mechanisms, combining the data in Tables 5 and 6.

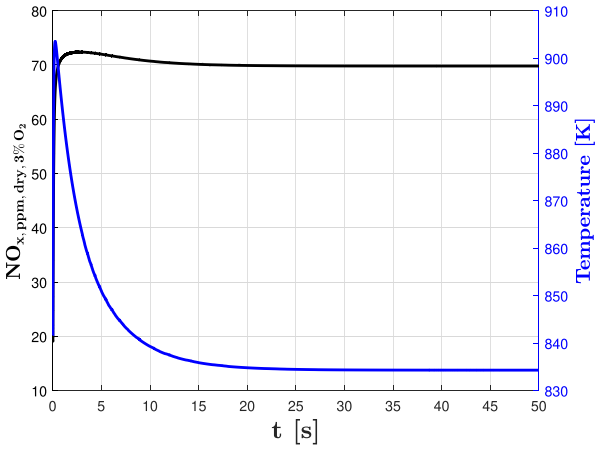

Fig. 18. In black the trend of NO_x and in blue the trend of the static temperature inside PSR6 as time varies. The graph shows a simulation reaching steady state, specifically for PSR 6 with a water loading of 0% using the Creck mechanism.

3×10^{-3} CPU hours per simulation on a 12th Gen Intel(R) Core(TM) i7-1255U processor.

Finally, the predictive capability of the reactor network for varying water injection rates is shown in Fig. 20. The figure illustrates NO_x concentrations (expressed in ppm dry at 3% O_2) as a function of water mass fraction (Y_{H_2O}) in the inlet stream. The CRN prediction curve shows excellent agreement with the discrete CFD data points across the entire range of water loadings examined. As water content increases from 0% to 15%, NO_x emissions decrease exponentially, dropping from approximately 70 ppm to near-zero levels. This result confirms that the reactor network serves as a computationally efficient alternative to resource-intensive CFD simulations, while maintaining high accuracy in predicting emission trends under various water injection conditions.

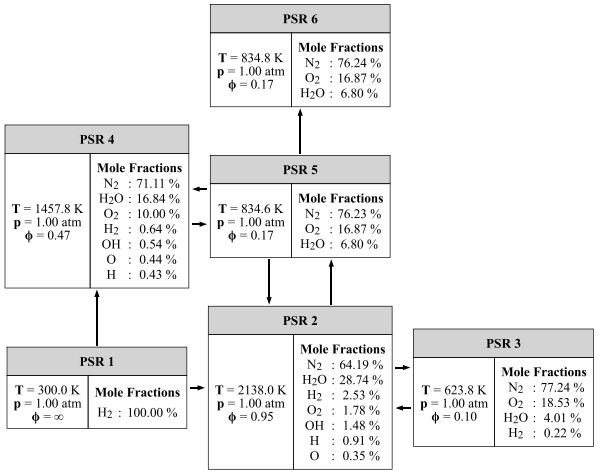

Fig. 19. Reactor network at steady-state condition utilizing the Creck chemical kinetic mechanism with 0% water loading. The diagram illustrates the six interconnected reactors with their corresponding thermodynamic properties (temperature T, pressure p, equivalence ratio ϕ) and major species composition (expressed as mole fractions). Minor species with mole fractions below 0.1% are omitted from the representation for clarity.

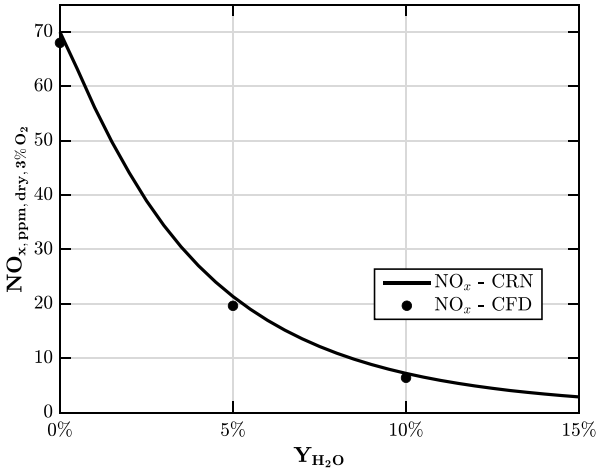

Fig. 20. The solid black line shows the NO_x ppm dry computed via the CRN while the dots show the CFD prediction. The NO_x emissions measured experimentally with Y_{H_2O} = 0% are 70 ppm.

It is worth noting that, in this work, the CRN data for water injection cases have been validated exclusively against CFD results, with the network trained using only a single experimental data point corresponding to the case without water injection. This choice is not intended to circumvent experimental validation, but rather reflects the practical limitations that often constrain the availability of high-fidelity or experimental data. In such contexts, it becomes essential to maximize the utility of the limited data available. The CRN-based approach developed here is particularly well-suited for these scenarios: by partitioning the simulated domain into a limited number of subdomains based on macroscopic flow behavior, it enables accurate approximations even with sparse validation data, leveraging the available information through the optimization procedure. Furthermore, provided that the overall flow structure remains relatively insensitive to variations such as steam injection, the model can be reliably extended to explore operating conditions beyond the validation point. In the burner configuration studied here, this relative insensitivity of the velocity field to water injection is demonstrated in Figs. 15 and 16, which present radial profiles of the velocity components in the burner section intersecting the flame.

5. Conclusions

This study examined the use of steam injection as a viable option for NO_x emissions abatement. As mentioned in the introduction, this technique has been explored in the aerospace sector to enhance performance during critical phases, such as takeoff. The study initially focused on analyzing a counterflow diffusive flame configuration. This standard academic configuration was chosen because it hints the steam's effectiveness in reducing emissions through computationally inexpensive simulations. However, despite the low computational cost and the similar phenomenology depicted, the capability of these simulations to quantitatively predict emissions and the reduction of NO_x levels due to water addition in practical scenarios remains limited. For this reason, a realistic configuration used in an experimental setup was considered, and a CFD numerical framework was developed and validated to accurately capture emissions. Simultaneously, a new methodology for developing CRNs was proposed, with results validated through both experiments and CFD simulations. The following conclusions can be drawn from the present study:

- Although the counterflow setup can predict the qualitative effects of steam addition on emission reduction, it is unable to quantitatively estimate the pollutant reductions observed in the burner configuration.
- Steam injection has demonstrated its ability to reduce NO_x emissions in the burner configuration, even when the exit temperature is kept constant, which was regulated by adjusting the overall equivalence ratio. The NO_x emissions exhibit a monotonically decreasing trend, even at very high levels of steam injection.
- The RANS methodology employed in this study accurately captures NO_x emissions, as demonstrated by comparisons with experimental data obtained without steam addition. Moreover, this predictive capability is consistent across multiple chemical mechanisms, with both the Creck and Naik mechanisms yielding results within the experimental standard deviation. However, the limitations of this numerical framework have not been fully explored; thus, under design conditions that deviate significantly from the nominal case (i.e., with high water loading), the results should be interpreted with caution.
- The novelty of the proposed methodology for developing the CRN lies in the use of an optimization algorithm to adjust the mass flow rates between the reactors, ensuring the correct level of emissions is captured.
- The CRNs designed using the proposed methodology have demonstrated the ability to accurately predict emission trends, even under conditions far from the training conditions. The results obtained with the CRNs closely match the trends computed by the CFD, but at a significantly lower computational cost.
- The CRN results, computed at high steam addition levels, perfectly follow the strongly non-linear trend that can be extrapolated from the CFD simulations.

Using CRNs significantly reduces computational costs during the design phase, and the network developed with the current methodology can be easily integrated into system simulation frameworks, such as the Numerical Propulsion System Simulation (NPSS) [68], ensuring a faster and more cost-effective design process. Future research could explore the application of liquid water injection and expand the use of the CRN methodology to a wider range of test cases to validate its effectiveness in different combustion environments. Additionally, although the reactor network approach already offers a substantial computational

advantage, achieving speedups of several orders of magnitude compared to CFD, future work could focus on refining the optimization strategy. This would be particularly beneficial for more complex combustor configurations or significantly different flow topologies, where the training cost may become more demanding.

Nomenclature

Roman symbols

Symbol	Description	Units
A	Energy transfer due to conduction	W m^{-2}
a	Strain rate in counterflow flames	s^{-1}
$a_{0,j}$		–
$a_{1,j}$	NASA7 polynomial coefficients	K^{-1}
$a_{2,j}$	for species j	K^{-2}
$a_{3,j}$		K^{-3}
$a_{4,j}$		K^{-4}
B	Energy transfer due to viscous dissipation	W m^{-2}
C	Energy transfer due to species enthalpy diffusion	W m^{-2}
C_τ	Time scale constant in EDC model	–
C_ξ	Fine-structure region constant in EDC model	–
c_1	Cognitive acceleration coefficient in PSO	–
c_2	Social acceleration coefficient in PSO	–
c_p	Mixture specific heat capacity at constant pressure	J kg^{-1} K^{-1}
$c_{p,j}$	Specific heat capacity of species j at constant pressure	J kg^{-1} K^{-1}
$\hat{c}_{p,j}$	Molar heat capacity of species j at constant pressure	J mol^{-1} K^{-1}
c_v	Mixture specific heat capacity at constant volume	J kg^{-1} K^{-1}
$D_{j,m}$	Molecular mass diffusion coefficient of species j	m^2 s^{-1}
$D_{T,j}$	Soret diffusion coefficient of species j	kg m^{-1} s^{-1}
d	Inlet distance in counterflow flames	m
E	Sum of specific internal and kinetic energy	J kg^{-1}
e	Total specific internal energy	J kg^{-1}
e_j	Total specific internal energy of species j	J kg^{-1}
g_{best}	Global best position in PSO	–
H	Total specific enthalpy	J kg^{-1}
h	Sensible specific enthalpy	J kg^{-1}
h_j	Sensible specific enthalpy of species j	J kg^{-1}
h_j^0	Enthalpy of formation of species j for unit mole	J mol^{-1}
h_{in}	Specific enthalpy of inlet stream	J kg^{-1}
$\vec{J}_j$	Diffusion flux of species j	kg m^{-2} s^{-1}
k	Thermal conductivity	W m^{-1} K^{-1}
k_{eff}	Effective thermal conductivity	W m^{-1} K^{-1}
M	Total number of species in mixture	–
m	Mass	kg
$\mathcal{M}_j$	Molecular weight of species j	kg mol^{-1}
$\dot{m}$	Mass flow rate	kg s^{-1}
$\dot{m}_{Air_{tot}}$	Total air mass flow rate	kg s^{-1}
$\dot{m}_{Air_I}$	Mass flow rates in CRN model	kg s^{-1}
$\dot{m}_{Air_{II}}$		kg s^{-1}
$\dot{m}_A$		kg s^{-1}
$\dot{m}_B$		kg s^{-1}
$\dot{m}_C$		kg s^{-1}
$\dot{m}_D$		kg s^{-1}
$\dot{m}_E$		kg s^{-1}
$\dot{m}_F$		kg s^{-1}
$\dot{m}_G$		kg s^{-1}
$\dot{m}_I$		kg s^{-1}
$\dot{m}_{H_{2,tot}}$	Total hydrogen mass flow rate	kg s^{-1}
$\dot{m}_{in}$	Inlet mass flow rate	kg s^{-1}
$\dot{m}_{j,gen}$	Mass generation rate of species j	kg s^{-1}
$\dot{m}_{out}$	Outlet mass flow rate	kg s^{-1}
p	Pressure	Pa
p_k	Position of kth particle in PSO	–
$p_{k,best}$	Personal best position of kth particle in PSO	–
$\mathcal{P}_1$	CRN model parameters	–
$\mathcal{P}_2$		–
$\mathcal{P}_3$		–
$\mathcal{P}_4$		–
$\mathcal{P}^{opt}$	Optimized parameter set	–
Pr_t	Turbulent Prandtl number	–
r	Radial coordinate	m
r_1, r_2	Random numbers in PSO algorithm	–
R	Universal gas constant	J mol^{-1} K^{-1}
R_b	Outer radius of the annular air passage	m
Re_{fuel}	Fuel jet Reynolds number	–
$\mathcal{R}_j$	Volumetric rate of formation of species j	kg m^{-3} s^{-1}
S	Swirl number	–
Sc_t	Turbulent Schmidt number	–
T	Static temperature	K
T_{ref}	Reference temperature	K
t	Time	s
u_j	Specific internal energy of species j	J kg^{-1}
V	Volume	m^3
v_k	Velocity of kth particle in PSO	–
v_x, v_r, v_θ	Velocity components (axial, radial, tangential)	m s^{-1}
$\vec{v}$	Velocity vector	m s^{-1}
w	Inertia weight in PSO	–
x	Axial coordinate	m
Y_j	Mass fraction of species j	–
$Y_{j,in}$	Mass fraction of species j in inlet stream	–
Y_j^*	Fine-scale mass fraction of species j after reaction	–

Greek symbols

Symbol	Description	Units
ϵ	Rate of dissipation of turbulent kinetic energy	m^2 s^{-3}
κ	Turbulent kinetic energy	m^2 s^{-2}
κ_{fs}	Volume fraction of fine scales	–
μ	Dynamic viscosity	Pa s
μ_t	Turbulent viscosity	Pa s
ν	Kinematic viscosity	m^2 s^{-1}
ξ	Fine-structure region mass fraction	–

ρ	Density	kg m^{-3}
$\hat{\tau}$	Total stress tensor	Pa
τ^*	Fine-scale time scale	s
ϕ	Equivalence ratio	–
ω	Specific dissipation rate	s^{-1}
Ω	Heat generation from chemical reactions	W m^{-3}

Mathematical operators and special symbols

Symbol	Description
$\overline{(\cdot)}$	Reynolds-averaged quantity
$\widetilde{(\cdot)}$	Favre-averaged quantity
$\vec{r}$	Unit vector in radial direction
$\vec{x}$	Unit vector in axial direction
∇	Nabla operator

Abbreviations and acronyms

Abbreviation	Definition
CFD	Computational Fluid Dynamics
CRN	Chemical Reactor Network
EDC	Eddy-Dissipation Concept
GA	Genetic Algorithm
MUSCL	Monotonic Upstream-centered Scheme for Conservation Laws
NASA7	NASA 7-coefficient polynomial
PRESTO!	PREssure STaggering Option
PSO	Particle Swarm Optimization
PSR	Perfectly Stirred Reactor
RANS	Reynolds-Averaged Navier–Stokes
SST	Shear Stress Transport
UDF	User-Defined Function

CRediT authorship contribution statement

Lorenzo Folcarelli: Writing – original draft, Visualization, Validation, Software, Methodology, Investigation, Formal analysis, Data curation, Conceptualization. **Riccardo Concetti:** Writing – original draft, Validation, Methodology, Investigation, Formal analysis, Conceptualization. **Fabio Cozzi:** Writing – review & editing. **Andrea Ferrero:** Writing – review & editing, Funding acquisition. **Filippo Masseni:** Writing – review & editing. **Dario Pastrone:** Writing – review & editing, Funding acquisition. **Josef Hasslberger:** Writing – review & editing, Supervision. **Markus Klein:** Writing – review & editing, Supervision, Resources, Funding acquisition.

Declaration of competing interest

The authors declare that they have no known competing financial interests or personal relationships that could have appeared to influence the work reported in this paper.

Acknowledgments

This publication is part of the project PNRR-NGEU, which has received funding from the Italian Ministry of University and Research (MUR) (Ministerial Decree 351/2022).

Riccardo Concetti gratefully acknowledges the support of project MORE, which is funded by dtec.bw – Digitalization and Technology Research Center of the Bundeswehr which we gratefully acknowledge. dtec.bw is funded by the European Union – NextGenerationEU.

The authors gratefully acknowledge the Gauss Centre for Supercomputing e.V. (www.gauss-centre.eu) for funding this project by providing computing time on the GCS Supercomputer SuperMUC-NG at Leibniz Supercomputing Centre (www.lrz.de).

References

[1] Oliveira AM, Beswick RR, Yan Y. A green hydrogen economy for a renewable energy society. Curr Opin Chem Eng 2021;33:100701. http://dx.doi.org/10.1016/j.coche.2021.100701.

[2] Falcone PM, Hiete M, Sapio A. Hydrogen economy and sustainable development goals: Review and policy insights. Curr Opin Green Sustain Chem 2021;31:100506. http://dx.doi.org/10.1016/j.cogsc.2021.100506.

[3] Xu P, Ji C, Wang S, Cong X, Ma Z, Tang C, et al. Effects of direct water injection on engine performance in a hydrogen (H2)-fueled engine at varied amounts of injected water and water injection timing. Int J Hydrog Energy 2020;45(24):13523–34. http://dx.doi.org/10.1016/j.ijhydene.2020.03.011.

[4] Cavaliere A, de Joannon M. Mild combustion. Prog Energy Combust Sci 2004;30(4):329–66. http://dx.doi.org/10.1016/j.pecs.2004.02.003.

[5] Göke S, Paschereit CO. Influence of steam dilution on nitrogen oxide formation in premixed methane/hydrogen flames. J Propuls Power 2013;29(1):249–60. http://dx.doi.org/10.2514/1.B34577.

[6] Göke S, Schimek S, Terhaar S, Reichel T, Göckeler K, Krüger O, et al. Influence of pressure and steam dilution on NO x and CO emissions in a premixed natural gas flame. J Eng Gas Turbines Power 2014;136(9):091508. http://dx.doi.org/10.1115/1.4026942.

[7] Lellek S, Sattelmayer T. NOx-formation and CO-burnout in water-injected, premixed natural gas flames at typical gas turbine combustor residence times. J Eng Gas Turbines Power 2018;140(5):051504. http://dx.doi.org/10.1115/1.4038239.

[8] Görgülü A, Yağlı H, Koç Y, Koç A. Comprehensive analysis of the effect of water injection on performance and emission parameters of the hydrogen fuelled recuperative and non-recuperative gas turbine system. Int J Hydrog Energy 2020;45(58):34254–67. http://dx.doi.org/10.1016/j.ijhydene.2020.09.038.

[9] Kaiser S, Schmitz O, Ziegler P, Klingels H. The water-enhanced turbofan as enabler for climate-neutral aviation. Appl Sci 2022;12(23):12431. http://dx.doi.org/10.3390/app122312431.

[10] Advanced Research Projects Agency - Energy. Hydrogen Steam and Inter-Cooled Turbine Engine (HYSITE). 2022, URL: https://arpa-e.energy.gov/programs-and-initiatives/search-all-projects/hydrogen-steam-and-inter-cooled-turbine-engine-hysite. [Accessed 12 March 2025].

[11] Gai G, Kudriakov S, Rogg B, Hadjadj A, Studer E, Thomine O. Numerical study on laminar flame velocity of hydrogen-air combustion under water spray effects. Int J Hydrog Energy 2019;44(31):17015–29. http://dx.doi.org/10.1016/j.ijhydene.2019.04.225.

[12] Hasslberger J, Ozel-Erol G, Chakraborty N, Klein M, Cant S. Physical effects of water droplets interacting with turbulent premixed flames: a direct numerical simulation analysis. Combust Flame 2021;229:111404. http://dx.doi.org/10.1016/j.combustflame.2021.111404.

[13] Hasslberger J, Concetti R, Chakraborty N, Klein M. Inertial effects on the interaction of water droplets with turbulent premixed flames: A direct numerical simulation analysis. Proc Combust Inst 2023;39(2):2575–86. http://dx.doi.org/10.1016/j.proci.2022.07.039.

[14] Concetti R, Hasslberger J, Chakraborty N, Klein M. Analysis of water droplet interaction with turbulent premixed and spray flames using carrier phase direct numerical simulations. Combust Sci Technol 2023;195(7):1411–33. http://dx.doi.org/10.1080/00102202.2023.2182192.

[15] Concetti R, Hasslberger J, Chakraborty N, Klein M. Effects of liquid water addition on turbulent premixed hydrogen/air combustion. Fuel 2024;373:132314. http://dx.doi.org/10.1016/j.fuel.2024.132314.

[16] Concetti R, Hasslberger J, Sattelmayer T, Klein M. On the chemical effect of steam addition to premixed hydrogen flames with respect to NOx emissions and flame speed. Flow, Turbul Combust 2024;1–16. http://dx.doi.org/10.1007/s10494-024-00551-5.

[17] Koroll G, Mulpuru S. The effect of dilution with steam on the burning velocity and structure of premixed hydrogen flames. In: Symposium (international) on combustion, vol. 21, (no. 1):Elsevier; 1988, p. 1811–9. http://dx.doi.org/10.1016/S0082-0784(88)80415-6.

[18] Lamioni R, Lapenna PE, Berger L, Kleinheinz K, Attili A, Pitsch H, et al. Pressure-induced hydrodynamic instability in premixed methane-air slot flames. Combust Sci Technol 2020;192(11):1998–2009. http://dx.doi.org/10.1080/00102202.2020.1768081.

[19] Attili A, Lamioni R, Berger L, Kleinheinz K, Lapenna PE, Pitsch H, et al. The effect of pressure on the hydrodynamic stability limit of premixed flames. Proc Combust Inst 2021;38(2):1973–81. http://dx.doi.org/10.1016/j.proci.2020.06.091.

[20] Lyu Y, Qiu P, Liu L, Yang C, Sun S. Effects of steam dilution on laminar flame speeds of H2/air/H2O mixtures at atmospheric and elevated pressures. Int J Hydrog Energy 2018;43(15):7538–49. http://dx.doi.org/10.1016/j.ijhydene.2018.02.065.

[21] Adler EJ, Martins JR. Hydrogen-powered aircraft: Fundamental concepts, key technologies, and environmental impacts. Prog Aerosp Sci 2023;141:100922. http://dx.doi.org/10.1016/j.paerosci.2023.100922, Special Issue on Green Aviation.

[22] Faravelli T, Bua L, Frassoldati A, Antifora A, Tognotti L, Ranzi E. A new procedure for predicting NOx emissions from furnaces. Comput Chem Eng 2001;25(4–6):613–8. http://dx.doi.org/10.1016/S0098-1354(01)00641-X.

[23] Fichet V, Kanniche M, Plion P, Gicquel O. A reactor network model for predicting NOx emissions in gas turbines. Fuel 2010;89(9):2202–10. http://dx.doi.org/10.1016/j.fuel.2010.02.010.
[24] Innocenti A, Andreini A, Bertini D, Facchini B, Motta M. Turbulent flow-field effects in a hybrid CFD-CRN model for the prediction of NOx and CO emissions in aero-engine combustors. Fuel 2018;215:853–64. http://dx.doi.org/10.1016/j.fuel.2017.11.097.
[25] Romano C, Cerutti M, Babazzi G, Miris L, Lamioni R, Galletti C, et al. Ammonia blends for gas-turbines: Preliminary test and CFD-CRN modelling. Proc Combust Inst 2024;40(1–4):105494. http://dx.doi.org/10.1016/j.proci.2024.105494.
[26] Nguyen TH, Kim S, Park J, Jung S, Kim S. CFD-CRN validation study for NO x emission prediction in lean premixed gas turbine combustor. J Mech Sci Technol 2017;31:4933–42. http://dx.doi.org/10.1007/s12206-017-0942-2.
[27] De Toni A, Hayashi T, Schneider P. A reactor network model for predicting NOx emissions in an industrial natural gas burner. J Braz Soc Mech Sci Eng 2013;35:199–206. http://dx.doi.org/10.1007/s40430-013-0039-5.
[28] Yousefian S, Bourque G, Monaghan RF. Bayesian inference and uncertainty quantification for hydrogen-enriched and lean-premixed combustion systems. Int J Hydrog Energy 2021;46(46):23927–42. http://dx.doi.org/10.1016/j.ijhydene.2021.04.153.
[29] Mao G, Shi T, Mao C, Wang P. Prediction of NOx emission from two-stage combustion of NH3–H2 mixtures under various conditions using artificial neural networks. Int J Hydrog Energy 2024;49:1414–24. http://dx.doi.org/10.1016/j.ijhydene.2023.10.129.
[30] Vance FH, De Goey L, van Oijen JA. Development of a flashback correlation for burner-stabilized hydrogen-air premixed flames. Combust Flame 2022;243:112045. http://dx.doi.org/10.1016/j.combustflame.2022.112045.
[31] Reichel TG, Paschereit CO. Interaction mechanisms of fuel momentum with flashback limits in lean-premixed combustion of hydrogen. Int J Hydrog Energy 2017;42(7):4518–29. http://dx.doi.org/10.1016/j.ijhydene.2016.11.018.
[32] Mira D, Lehmkuhl O, Both A, Stathopoulos P, Tanneberger T, Reichel TG, et al. Numerical characterization of a premixed hydrogen flame under conditions close to flashback. Flow, Turbul Combust 2020;104:479–507. http://dx.doi.org/10.1016/j.ijhydene.2016.11.018.
[33] Aniello A, Poinsot T, Selle L, Schuller T. Hydrogen substitution of natural-gas in premixed burners and implications for blow-off and flashback limits. Int J Hydrog Energy 2022;47(77):33067–81. http://dx.doi.org/10.1016/j.ijhydene.2022.07.066.
[34] Cozzi F, Coghe A. Behavior of hydrogen-enriched non-premixed swirled natural gas flames. Int J Hydrog Energy 2006;31(6):669–77. http://dx.doi.org/10.1016/j.ijhydene.2005.05.013.
[35] Gupta AK, Syred N, Lilley DG. Swirl flows. In: Energy and engineering science series, Tunbridge Wells, Kent: Abacus Press; 1984.
[36] Goodwin DG, Moffat HK, Schoegl I, Speth RL, Weber BW. Cantera: An object-oriented software toolkit for chemical kinetics, thermodynamics, and transport processes. 2023, http://dx.doi.org/10.5281/zenodo.8137090, Version 3.0.0, https://www.cantera.org.
[37] Kee RJ, Coltrin ME, Glarborg P. Chemically reacting flow: theory and practice. John Wiley & Sons; 2005, http://dx.doi.org/10.1002/0471461296.
[38] Fiala T, Sattelmayer T. Nonpremixed counterflow flames: scaling rules for batch simulations. J Combust 2014;2014(1):484372. http://dx.doi.org/10.1155/2014/484372.
[39] Acheson DJ. Elementary fluid dynamics. Oxford University Press; 1990.
[40] Ansys, Inc. Ansys fluent theory guide. 2024, Version 2024R1.
[41] Menter FR. Two-equation eddy-viscosity turbulence models for engineering applications. AIAA J 1994;32(8):1598–605. http://dx.doi.org/10.2514/3.12149.
[42] McBride BJ, Gordon S, Reno MA. Coefficients for calculating thermodynamic and transport properties of individual species, vol. 4513, NASA Langley Research Center; 1993, https://ntrs.nasa.gov/citations/19940013151.
[43] Magnussen BF. The eddy dissipation concept: A bridge between science and technology. In: ECCOMAS thematic conference on computational combustion, vol. 21, 2005, p. 24, https://api.semanticscholar.org/CorpusID:67818474.
[44] Gran IR, Magnussen BF. A numerical study of a bluff-body stabilized diffusion flame. Part 2. Influence of combustion modeling and finite-rate chemistry. Combust Sci Technol 1996;119(1–6):191–217. http://dx.doi.org/10.1080/00102209608951999.
[45] Ertesvåg IS. Scrutinizing proposed extensions to the Eddy Dissipation Concept (EDC) at low turbulence Reynolds numbers and low Damköhler numbers. Fuel 2022;309:122032. http://dx.doi.org/10.1016/j.fuel.2021.122032.
[46] Patankar S. Numerical heat transfer and fluid flow. 1st ed. Boca Raton: CRC Press; 1980, http://dx.doi.org/10.1201/9781482234213.
[47] Barth T, Jespersen D. The design and application of upwind schemes on unstructured meshes. In: 27th aerospace sciences meeting. 1989, http://dx.doi.org/10.2514/6.1989-366.
[48] van Leer B. Towards the ultimate conservative difference scheme. V. A second-order sequel to godunov's method. J Comput Phys 1979;32(1):101–36. http://dx.doi.org/10.1016/0021-9991(79)90145-1.
[49] Rossiello G, Uzair MA, Ahmadpanah SB, Morandi L, Ferrara M, Rago GD, et al. Design and testing of a Multi-Fuel industrial burner suitable for syngases, flare gas and pure hydrogen. Therm Sci Eng Prog 2023;42:101845. http://dx.doi.org/10.1016/j.tsep.2023.101845.
[50] Kumar A, Bharti RP. Assessment of RANS-based turbulence models for isothermal confined swirling flow in a realistic can-type gas turbine combustor application. J Comput Sci 2024;81:102362. http://dx.doi.org/10.1016/j.jocs.2024.102362.
[51] Kennedy J, Eberhart R. Particle swarm optimization. In: Proceedings of ICNN'95-international conference on neural networks, vol. 4, IEEE; 1995, p. 1942–8. http://dx.doi.org/10.1109/ICNN.1995.488968.
[52] Casalino L, Masseni F, Pastrone D. Robust design approaches for hybrid rocket upper stage. J Aerosp Eng 2019;32(6):04019087. http://dx.doi.org/10.1061/(ASCE)AS.1943-5525.000107.
[53] Trelea IC. The particle swarm optimization algorithm: Convergence analysis and parameter selection. Inform Process Lett 2003;85(6):317–25. http://dx.doi.org/10.1016/S0020-0190(02)00447-7.
[54] Naik CV. Detailed mechanism for hydrogen combustion with NOx. Ansys, Inc.; 2009, Originally developed by Reaction Design, now part of Ansys.
[55] Gotama GJ, Hayakawa A, Okafor EC, Kanoshima R, Hayashi M, Kudo T, et al. Measurement of the laminar burning velocity and kinetics study of the importance of the hydrogen recovery mechanism of ammonia/hydrogen/air premixed flames. Combust Flame 2022;236:111753. http://dx.doi.org/10.1016/j.combustflame.2021.111753.
[56] Song Y, Marrodán L, Vin N, Herbinet O, Assaf E, Fittschen C, et al. The sensitizing effects of NO2 and NO on methane low temperature oxidation in a jet stirred reactor. Proc Combust Inst 2019;37(1):667–75.
[57] Stagni A, Cavallotti C, Arunthanayothin S, Song Y, Herbinet O, Battin-Leclerc F, et al. An experimental, theoretical and kinetic-modeling study of the gas-phase oxidation of ammonia. React Chem Eng 2020;5(4):696–711.
[58] Stagni A, Arunthanayothin S, Dehue M, Herbinet O, Battin-Leclerc F, Bréquigny P, et al. Low- and intermediate-temperature ammonia/hydrogen oxidation in a flow reactor: Experiments and a wide-range kinetic modeling. Chem Eng J 2023;471:144577. http://dx.doi.org/10.1016/j.cej.2023.144577.
[59] Cameretti MC, De Robbio R, Ferrara V, Tuccillo R. Performance and emissions evaluation of a turbofan burner with hydrogen fuel. Aerospace 2025;12(3). http://dx.doi.org/10.3390/aerospace12030231.
[60] Babazzi G, Gauthier PQ, Agarwal P, McClure J, Sethi V. NOx emissions predictions for a hydrogen micromix combustion system. In: Turbo expo: power for land, sea, and air, vol. 58608, American Society of Mechanical Engineers; 2019, http://dx.doi.org/10.1115/GT2019-90532, p. V003T03A008.
[61] Lamioni R, Mariotti A, Salvetti MV, Galletti C. Chemical reactor network modeling of ammonia–hydrogen combustion in a gas turbine: stochastic sensitivity analysis. Appl Therm Eng 2024;244:122734. http://dx.doi.org/10.1016/j.applthermaleng.2024.122734.
[62] Jin U, Kim KT. Hybrid rich- and lean-premixed ammonia-hydrogen combustion for mitigation of NOx emissions and thermoacoustic instabilities. Combust Flame 2024;262:113366. http://dx.doi.org/10.1016/j.combustflame.2024.113366.
[63] Jamshidiha M, Kamal M, Cafiero M, Coussement A, Parente A. Experimental and numerical characterization of hydrogen combustion in a reverse-flow micro gas turbine combustor. Int J Hydrog Energy 2024;55:1299–311. http://dx.doi.org/10.1016/j.ijhydene.2023.11.243.
[64] Lu C, Zhang L, Cao C, Chen X, Xing C, Shi H, et al. The effects of N2 and steam dilution on NO emission for a H2/Air micromix flame. Int J Hydrog Energy 2022;47(63):27266–78. http://dx.doi.org/10.1016/j.ijhydene.2022.06.050.
[65] Lu C, Zhang L, Xing C, Liu L, Qiu P. Effects of characteristic diameter, steam dilution, and equivalence ratio on NO formation for a H2/Air micromix design. Int J Hydrog Energy 2024;61:1133–41. http://dx.doi.org/10.1016/j.ijhydene.2024.02.373.
[66] Lyu Y, Aspden A, Zhang L, Liu L, Qiu P. Study of the chemical effect of steam dilution on NO formation in laminar premixed H2/Air flame at normal and elevated pressure. Int J Hydrog Energy 2021;46(24):13402–12. http://dx.doi.org/10.1016/j.ijhydene.2021.01.133.
[67] Palulli R, Zhang K, Dybe S, Yasir M, Paschereit CO, Duwig C. Investigation of NO formation in non-premixed, swirl-stabilised, wet hydrogen/air gas turbine combustor. Fuel 2024;378:132943. http://dx.doi.org/10.1016/j.fuel.2024.132943.
[68] Folcarelli L, Gedda G, Zumbo A, Ferrero A, Masseni F, Pastrone D. Integrated numerical modeling of a hydrogen turbofan engine and fuel system with alternative thermodynamic cycles. In: American institute of aeronautics and astronautics SciTech 2025 forum. 2025, http://dx.doi.org/10.2514/6.2025-0328.